
Wesleyan ♦ University

Occupation Statistics for an Atomic Bose-Einstein Condensate
in a Double Well Potential

By

Katrina Anne Smith-Mannschott

Faculty Advisor: Dr. Tsampikos Kottos

A Thesis submitted to the Faculty of Wesleyan University in partial fulfillment of the
requirements of the degree of Masters of Arts

Middletown, Connecticut

May 2009

Abstract

In this thesis we consider an atomic Bose-Einstein condensate (BEC) loaded in a biased double well potential trap with tunneling rate k and interatomic interaction U . The BEC is prepared such that all N atoms begin in one well. We drive the system by steadily changing the potential difference ε between the two wells. The driving of the system generates many-body Landau-Zener transitions which lead to a redistribution of the atomic population. We have investigated not only the first moment of the evolving occupation statistics, but all its moments, in particular, its variance. Our analysis indicates that depending on the interaction $u = NU/k$ and the sweep rate $\dot{\varepsilon}$, one can distinguish between three dynamical regimes: adiabatic, diabatic, and sudden. The analysis goes beyond the mean-field theory calculations used in the existing literature and is complemented by a semiclassical picture. We expect that our results will also shed light on the related area of mesoscopic electronics, where the problem of counting statistics is of great importance.

Acknowledgments

I would like to recognize and thank those who made writing this thesis possible.

I would like to thank Tsampikos Kottos for providing me the opportunity to work in his group. He has a great passion for his work and never seems to tire of answering questions, no matter how big or small.

Thank you also to Moritz Hiller, who helped me throughout my Senior as well as this Masters Thesis. He has taught me so much about physics and has always been very patient when I fumble.

Additionally, I am grateful to the others with whom we collaborated on this project: Doron Cohen and Maya Chuchem. Without their work and discussion, this thesis would have never been possible. I also acknowledge the support of the US-Israel Binational Science Foundation (BSF) and the Deutsche Forschungsgemeinschaft via the Forschergruppe 760.

Thank you to all the members of the Complex Quantum Dynamics and Mesoscopic Phenomena Group at Wesleyan University: Joshua Bodyfelt, Carl West, Mei Chai Zheng, James Aisenberg, and Charles and David Puelz. They have provided both valuable insights and amusing distractions.

I would like to recognize all of the professors from the physics department. From my first visit at Wesleyan to the present, I have felt welcomed and supported by everyone. I have enjoyed many wonderful classes and have gotten some sound advice. The open-door policy in the physics department has enriched my learning experience at Wesleyan by allowing me to explore questions, whether they be about a class or about my future in physics, with any member of the faculty. Thank you very much.

My friends from home (AK, Erin, Mary, Sasha, Steve, and Susan), as well as my friends Wesleyan (especially last year's housemates, Diana, Maya, Mel, and the "adopted" Theo, but also including all of the Air Fortress Ohio pack), have been very tolerant and encouraging during my studies. Thanks to Rachel Brown and Henny Admoni, who, also BA/MA students, commiserated with me regularly.

I would also like to thank my family. My mother, Elisabeth Mannschott, provided vital emotional, as well as financial, support during this time. Benjamin Smith-Mannschott, my brother, and Cynthia Volkert, my cousin, have both been very useful sounding boards, helping me calm the terror which is "Now what do I want to do?". I would like to acknowledge my father as well, though his death prevented him from being a part of my career at Wesleyan University, our shared humor has gotten me through many difficult days this year.

And last, but not least, thanks to Alexander Foss. He has an impressive ability to make me laugh even at the most stressful times and also to help me stay focused when I am driven to distraction. His patience and love helped me stay even-keeled throughout this entire process.

Contents

1	Introduction	1
2	Cold Bosons Interacting on a Lattice	4
2.1	Bose-Einstein Condensation	4
2.2	Optical Lattices	10
2.3	Bose-Hubbard Hamiltonian	13
2.4	The Classical Limit of the BHH and the Discrete Nonlinear Schrödinger Equation	15
2.5	Bose-Hubbard Dimer	17
2.6	The Heidelberg Experiment	18
3	Dynamics of the Symmetric Dimer	21
3.1	Wavepacket Dynamics: Quantum Calculations	21
3.2	Dimer in SU(2) Formalism	25
3.3	Classical Considerations	27
3.4	Characteristic Frequencies of the Classical Dynamics	31
3.5	Semiclassical Analysis	34
4	Landau-Zener Transitions	40
4.1	Parametric Hamiltonians and their Applications	41
4.2	Adiabatic Approximation and Equations of Motion	43
4.3	Example: A spin in a magnetic field	47
5	Dynamics of the Driven Dimer	49
5.1	Motivations for Study	49
5.2	Mean-field Dynamics and Nonlinear Landau-Zener Tunneling	52
5.3	The Bose-Hubbard Hamiltonian Formalism	54
5.4	Dynamical Regimes	55
5.5	Results	58
6	Conclusions	67
A	Critical Bias	69
B	Classical Analysis of Wavepacket Dynamics	70
C	The Equivalence of Counting and Occupation Statistics in the Dimer	72
D	The Diabatic-Sudden Crossover	73

1 Introduction

Bose-Einstein condensation of ultra-cold atoms is a topic which currently is very popular, both in theoretical and experimental research. The most fascinating of these experimental accomplishments include the realization of Bose-Einstein condensation (BEC) of ultra-cold atoms in optical lattices [2, 9, 39] and the creation of “atom chips” [22], which have been suggested as potential building blocks for quantum information processing [42]. In addition, the experimental study of BEC allows for novel, concrete applications of quantum mechanics, such as atom interferometers [43], transistors [36] and atom lasers [21]. In fact, the emerging field of atomtronics, i.e. the atom analogue of electronic materials, devices, and circuits, is predicted to be able to provide much more powerful devices than solid state ones. Atomtronics can be controlled to an extraordinary degree of precision, with respect not only to the confining potential, but also to the strength of the interaction between atoms, their preparation, and the measurement of the atomic cloud.

The aim of this thesis is to investigate the occupation statistics of a BEC in a driven double well potential. This problem has been studied heavily by theoreticians in the last few years, but due to recent experiments [1], interest in it has significantly intensified. Nevertheless, the majority of published works are based on the mean-field approach. There are only a few studies that have made further progress within the framework of a full quantum mechanical treatment of the system [58, 34, 56]. However, they only focused on calculating the average occupation of the wells, due to the inherent complexity of the calculation of the total occupation statistics. This thesis undertakes to study the latter,

1 Introduction

providing a many-body occupation statistics theory for the first time.

This thesis is structured as follows:

- *Chapter 2* will set up the mathematical and physical framework for the description of bosons on an optical lattice. It will begin with a brief introduction of the history that led to the realization of Bose-Einstein condensation, including the basic concepts behind creating a BEC. Furthermore, it will discuss how the BEC can be manipulated using optical lattices. We then introduce the Bose-Hubbard Hamiltonian (BHH), which is the standard mathematical model used to describe a BEC in a deep optical lattice. We go on to discuss the classical limit of the BHH, known as the Discrete Nonlinear Schrödinger (DNLS) equation. Then we describe the BHH for the double well potential (dimer). Finally, we discuss some recent experimental work by the Heidelberg group (see Ref. [1, 37]), and emphasize its importance and relevance to our own studies.
- In *Chapter 3*, we analyze the wavepacket dynamics of a BEC in a symmetric dimer trap. We begin by exploring the quantum evolution of the atomic population, touching on time-dependent perturbation theory for two limits: the small coupling regime and the small interatomic interaction regime. We then analyze the classical limits of wavepacket dynamics. To this end, we provide an understanding of the phase space of our system. We end the chapter by incorporating a semiclassical calculation that captures the essential features of the quantum dynamics. Comparisons between the results of the quantum evolution and the semiclassical prediction indicate the strengths of the semiclassical method [11].
- In *Chapter 4*, we discuss the physics of one-body Landau-Zener transitions - a vital component in determining the behavior of systems which are described by a time-dependent (parametric) Hamiltonian, such as the driven dimer. We do our presentation in a general context, introducing a few driven systems that are described by a parametric Hamiltonian. Next, we discuss the equations of motion

1 Introduction

for a generic driven system. We then note how adiabaticity can be achieved in such a system. Finally, we go through a simple example of a two-level system and derive the Landau-Zener transition probability.

- *Chapter 5* will present and analyze the dynamics of a BEC in a driven double well potential. First, it will enumerate some of the motivations behind studying this problem. Then, utilizing the mean-field framework, we will extend the Landau-Zener theory reviewed in Chapter 4 to a nonlinear system. The quantum and semiclassical approach to the problem will be discussed next. Depending on a rescaled interatomic interaction strength, we will be able to predict various dynamical scenarios as they depend on the driving rate. We will end the chapter by comparing our numerical and theoretical findings, including a useful scaling relation between the average population and its variance. The resulting scaling theory highlights the influence of interatomic interactions on the noise associated with the transport of atoms between wells. It can also shed some light on the problem of counting statistics in mesoscopic electronics in the presence of many-body interactions. [47]

We expect that our results will guide ongoing experimental efforts of Bose-Einstein condensates loaded into driven double well potentials [16, 20, 30]. These efforts will be focused on atomtronics, where it is vitally necessary to understand all sources of noise and how to control it so as to achieve optimal atomic transport. We also hope that our many-body occupation statistics theory will inspire further understanding of counting statistics in the frame of mesoscopic electronics.

2 Cold Bosons Interacting on a Lattice¹

This chapter is dedicated to presenting a mathematical and physical foundation for this thesis. We begin with a brief summary of the history leading up to the realization of Bose-Einstein condensation. Next, in §2.2, we give a short overview of how optical lattices can be used to manipulate Bose-Einstein condensates. In §2.3, we present the Bose-Hubbard Hamiltonian in second quantization. We discuss the appropriate semiclassical limit of the BHH, thereby deriving the Discrete Nonlinear Schrödinger (DNLS) equation in §2.4. The BHH for the dimer is discussed in §2.5. Finally, we summarize a recent experiment done with a BEC in a double well potential.

2.1 Bose-Einstein Condensation

Bose-Einstein condensate (BEC) was conceptualized and then realized through the efforts of many different prominent physicists during the last century. The story begins with Wien's law, the formula which was used to describe black-body radiation until 1900. Wien's law stated that $u_\nu = \nu^3 f(\nu/T)$, where u_ν is the energy density and f is a function of frequency and temperature. It was empirically shown that f should have the form of an exponential, $a\nu^3 e^{-b\nu/tT}$. Max Planck, as stickler for theoretical analysis, began to try to derive Wien's Law in 1894. Approximating a system to be made up of many oscillators, Planck came to the conclusion that Wien's law was correct and presented his findings to the Prussian Academy of Sciences. Four months later, in October 1900, Heinrich Rubens and Ferdinand Kurlbaum experimentally showed that Wien's law

¹This chapter taken with slight revisions from my Honors Thesis [46].

2 Cold Bosons Interacting on a Lattice

fails for black-body radiation at low frequency and high temperature - while Wien's law indicated that as ν/T shrinks, $u_\nu \propto \nu^3$, experimental results showed that u_ν does, in fact, depend on temperature. Using these experimental results as a guide, Planck was able to derive what is known today as Planck's Law:

$$u_\nu = \frac{8\pi\nu^2}{c^3} \frac{\epsilon}{e^{\frac{\epsilon}{k_B T}} - 1} \quad (2.1)$$

where $\epsilon = h\nu$. In deriving his law of black-body radiation, Planck, as he later stated in a letter, "was ready to sacrifice every one of [his] previous convictions about physical laws," excepting the first two laws of thermodynamics, which he stated "must be upheld under all circumstances." [35] One of the previous convictions Planck sacrificed was his opposition to the use of statistics to derive physical laws. A key step in his derivation is the use of Ludwig Boltzmann's relation $S \propto \ln W$, where S is entropy and W is the probability of a system being in a given state. Since Planck did still have an aversion to the use of probabilities, he reinterpreted W as the number of different ways a total energy E , divided into "energy elements" of ϵ , could be distributed among a number of oscillators. He labeled these energy elements $\epsilon = h\nu$. Planck's original hope was to, after having used ϵ to come up with a law for black-body radiation, take the limit as $h \rightarrow 0$, making the energy continuous. However, he found that only with the energy elements in place, did his law match the experimental data. When later asked how he chose to incorporate energy quantization, he wrote "Briefly summarized, what I did can be described as simply an act of desperation...[The energy element] was purely a formal assumption." [35] Though Planck used the concept of energy quanta, he did not fully understand its implications for physics. It was Albert Einstein who emphasized the importance of quantum theory by publishing a series of papers, most notably his theory of light quanta (or photons) in 1905.

Though Planck's law of black-body radiation, published in 1900, was correct, he used Boltzmann's statistics incorrectly, so Einstein rederived it directly from Boltzmann's

2 Cold Bosons Interacting on a Lattice

statistics and Maxwell's equations and while doing so found that light was, in fact, quantized. In 1924, Satyendra Nath Bose then rederived Planck's law of black-body radiation again, except while treating light as corpuscles, rather than a wave, as Einstein had done. He assumed that each quantum energy state could be occupied by any number of photons, and thus derived Bose statistics [35]. After Bose's findings were rejected by the *Philosophical Magazine*, he sent them to Einstein, asking him to translate them to German and publish them in *Zeitschrift für Physik* [31]. Einstein extended Bose's quantum statistics for photons to a gas of indistinguishable particles. As the number of particles in such a system is conserved, Einstein had thus predicted a new type of phase transition at low temperatures, which came to be known as Bose-Einstein condensation [18, 19].

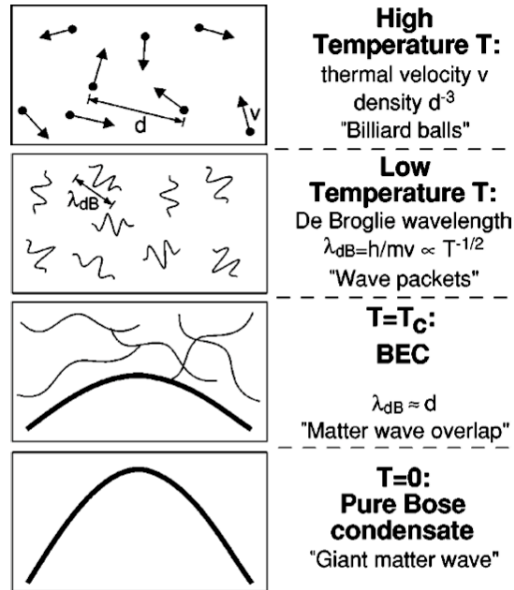


Figure 2.1: Criterion for Bose-Einstein condensation. At high temperatures, a weakly interacting gas can be treated as a system of "billiard balls." In a simplified quantum description, the atoms can be regarded as wavepackets with an extension of their de Broglie wavelength λ_{dB} . At the BEC transition temperature, λ_{dB} becomes comparable to the distance between atoms, and a Bose-Einstein condensate forms. As the temperature approaches zero, the thermal cloud disappears, leaving a pure Bose condensate. Figure from [29].

2 Cold Bosons Interacting on a Lattice

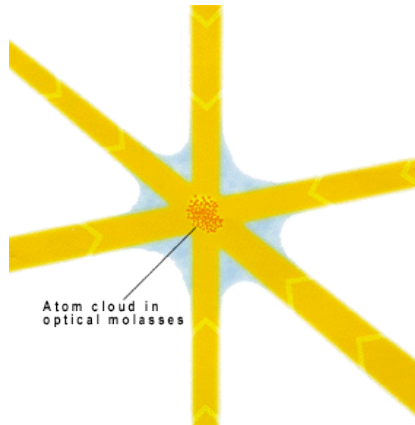


Figure 2.2: An illustration of optical molasses using six interfering lasers [38].

Einstein postulated that, like the photons described in Bose’s paper, integer spin (bosonic) atoms do not obey the Pauli exclusion principle, thus allowing an arbitrary number of identical bosons to pile up in the same quantum state. Einstein further speculated that when a cloud of bosons is cooled below a critical temperature, T_c , the atoms will condense down to the lowest energy quantum state. During this cooling process, the de Broglie wavelength $\lambda_{dB} = (2\pi\hbar^2/k_B m T)^{1/2}$ grows and thus the wavefunctions of the atoms smear and eventually overlap. This allows the wavefunction which describes the whole cloud of N bosons to reduce to a product of N identical single-particle ground state wavefunctions [52]. This process is illustrated in Fig. 2.1.

Though predicted in 1925, it was not until seventy years later that Bose-Einstein condensation was experimentally realized. The first two groups to observe an “ideal” BEC were the Wieman/Cornell group at the University of Colorado [3] and the Ketterle group at Massachusetts Institute of Technology [17]. Although creating a BEC may seem trivial - that is, making a cloud of bosons as cold as possible - in practice it proved to be quite difficult. Two substantial obstacles stood in the way of achieving a BEC. The first hinderance was that researchers had to ensure that as they lowered the temperature of the atom cloud, the gas did not transition to the more familiar phases: liquid and solid. This more conventional condensation can only be avoided at very low densities [29]. Thus researchers had to make certain that they were working with atoms which could be cooled to a BEC.

2 Cold Bosons Interacting on a Lattice

The second obstacle to realizing the BEC was figuring out how to trap and cool the atom cloud. Each time researchers got close to achieving a BEC, they ran into more technical difficulties. It was only in the 1980s that a breakthrough was made in laser cooling techniques by W.D. Phillips, S. Chu, and C. Cohen-Tannoudji, all of whom were awarded the Nobel Prize [13]. The laser cooling technique is based on the use of the Doppler effect. Counter propagating lasers, which are tuned to a frequency just below the resonance frequency of the atoms in the cloud, are set up to create a standing wave. The cloud of atoms is placed in this standing wave and at low intensities the atoms feel opposing forces from the lasers. These slow the atoms down (i.e. cool them) [14]. This technique is known as "optical molasses" (see Fig. 2.2). The problem with laser cooling is that the lowest reachable temperature is limited by the energy of a photon. Thus, while laser cooling can bring the atomic cloud down to the order of a few microkelvin, this is still too 'hot' to create a BEC [14]. Thus, a secondary cooling technique needed to be utilized.

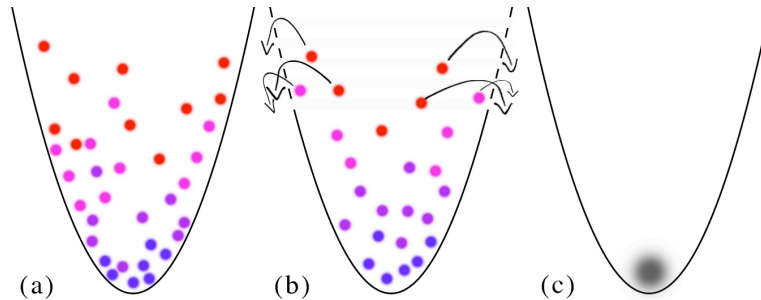


Figure 2.3: An illustration of evaporative cooling. (a) Atoms cooled via optical molasses are placed in trap. (b) Sides of trap are lowered to allow higher energy atoms to escape, leaving lower energy atoms behind. (c) After critical temperature T_c is achieved, the boson gas collapses into a Bose-Einstein condensate.

In the early 1980s, efforts were being made to Bose condense hydrogen atoms. They went through a two-step cooling process: (i) a dilution refrigerator and (ii) a magnetic trap with evaporative cooling. These experiments came very close to achieving BEC, but were hampered by the tendency of the atoms to recombine to form molecules [53].

2 Cold Bosons Interacting on a Lattice

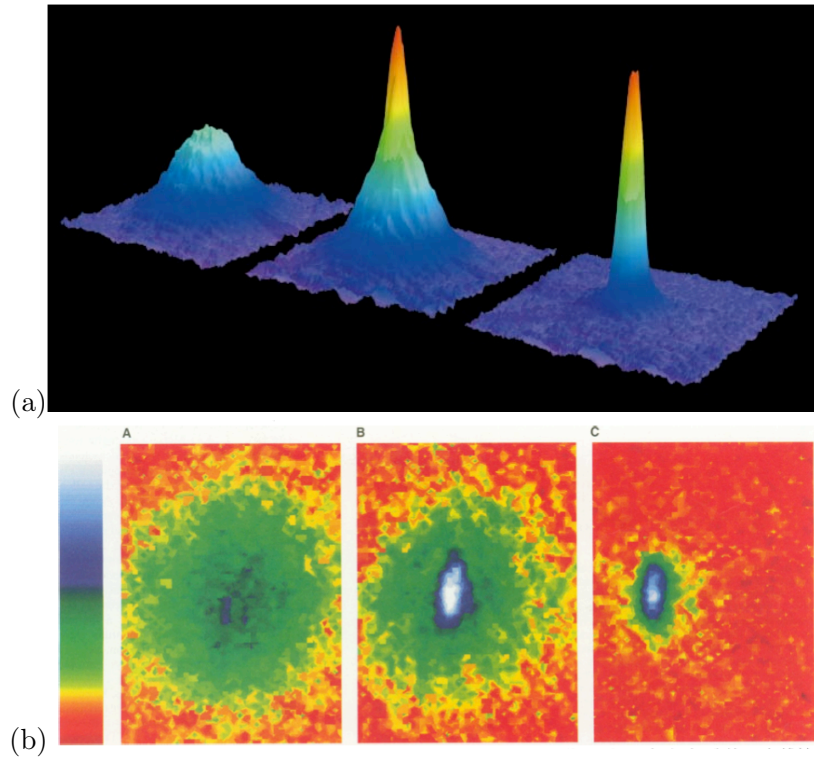


Figure 2.4: Observation of Bose-Einstein condensation by absorption imaging. Shown is absorption vs two spatial dimensions. The Bose-Einstein condensate is characterized by its slow expansion observed after 6 ms time of flight. The left picture shows an expanding cloud cooled to just about the transition point; middle: just after the condensate appeared; right: after further evaporative cooling has left an almost pure condensate. (a) The total number of atoms at the phase transition is about 7×10^5 , the temperature at the transition point is $2 \mu\text{K}$. Figure from [29]. (b) The circular pattern of the noncondensate fraction (mostly yellow and green) is an indication that the velocity distribution is isotropic, consistent with thermal equilibrium. The condensate fraction (mostly blue and white) is elliptical, indicative that it is highly nonthermal distribution. The elliptical pattern is in fact an image of a single, macroscopically occupied quantum wavefunction. The field of view of each image is $200 \mu\text{m}$ by $270 \mu\text{m}$. The observed horizontal width of the condensate is broadened by the experimental resolution. Figure from [3].

Wiemann/Cornell and Ketterle were able to achieve BEC because, rather than using either just laser cooling or just evaporative cooling, they combined them. They begin by using optical molasses to cool the atom cloud and then move the pre-cooled atom cloud into a magnetic trap [37]. Next, the trap depth is reduced, allowing the more energetic

(i.e. hotter) atoms to escape, while the colder atoms stay behind. The remaining atoms rethermalize and then the trap depth is reduced again. This is repeated until the atom cloud reaches 500nK to 2 μ K, at which point, the cloud collapses into a Bose-Einstein condensate [29] (See Fig. 2.3).² Thus, the University of Colorado and MIT groups were able to realize BEC (See Fig. 2.4).

It is worth noting the elliptical shape of the velocity distribution in Fig. 2.4b. In order to show that they had, indeed, achieved Bose-Einstein condensation, the Wiemann/Cornell and Ketterle groups needed to create a magnetic trap which had an elliptical horizontal cross section. Since the Heisenberg uncertainty principle states that we cannot simultaneously know precisely where a particle is and how fast it is going, $\Delta p \Delta x \geq \frac{\hbar}{2}$, we know that if we narrow down where the particle is spatially, our velocity distribution will spread, especially when in the ground state. Thus, by making the trap elliptical, the experimenters were able to observe when the gas fell into the ground state by the appearance of the elliptical velocity spread.

2.2 Optical Lattices

Since the BEC was achieved, many experimental developments have deepened our understanding of fundamental aspects of quantum physics. It simultaneously has allowed us to investigate complicated theoretical scenarios with potential technological applications. The most fascinating of these experimental achievements was the realization of Bose-Einstein condensation (BEC) of ultra-cold atoms in optical lattices (OL), which has been suggested as a potential building block for quantum information processing. At the same time the precise tailoring and manipulation of OLs has allowed us to investigate complex solid state phenomena, such as the Mott-Insulator to superfluid transition, the Josephson effect, the atom blockade phenomenon in quantum-dot-like potentials, Anderson localization, and Bose-Glass transitions. In fact, it is anticipated that the emerging

²An applet which provides a visual understanding of evaporative cooling is available at: <http://www.colorado.edu/physics/2000/applets/bec.html>. Last accessed: 2009-04-23. Applets demonstrating optical molasses and other steps in the experimental process also available here.

2 Cold Bosons Interacting on a Lattice

field of atomtronics will be able to provide much more powerful devices than the current solid-state ones, in which imperfections and decoherence quickly destroy the delicate quantum effects (see Ref. [37] and references therein).

During research into laser cooling techniques, it was found that the interfering lasers created an egg carton-like potential [37], which was then utilized to create what is known as an optical lattice. Optical lattices function on the basis of the AC Stark effect. The light field of the laser creates an oscillating electric field, which, in turn, induces an electrical dipole moment in each of the atoms in the BEC. An energy shift, ΔE , is created by the interaction of electric dipole moments of the atoms and the laser's electric field, $E(t)$. The energy shift is [37]

$$\Delta E = -\frac{1}{2}\alpha(\omega)\langle E^2(t)\rangle \quad (2.2)$$

where α is the polarizability of the atomic level which resonates at ω_0 . In ΔE , $\omega = \omega_0 + \Delta$, where Δ is the detuning of the light field from the resonant frequency of the atoms. The induced dipole moment, $D = \alpha(\omega)E$ [37], will be in phase with the electric field if the detuning is negative, i.e. $\omega < \omega_0$, thus minimizing the potential where the laser intensity is maximized. On the other hand, if the detuning is positive, i.e. $\omega_0 < \omega$, then the potential will be minimized where the laser intensity is minimized. The latter situation is easier to control in an experimental situation and thus is preferable.

The detuning, along with the peak intensity of the laser I_P , provides control over the depth of the lattice sites V_0 as [37]

$$V_0 \propto \frac{I_P}{\Delta} = \frac{I_P}{\omega - \omega_0} \quad (2.3)$$

Since we are working with a BEC, particle-particle collisions are estimated to have an energy transfer so small that none of the particles get excited into a higher energy level; thus the system remains in the ground state. When using an optical lattice to trap the BEC, spontaneous photon-particle scattering, i.e. photons pushing particles into a

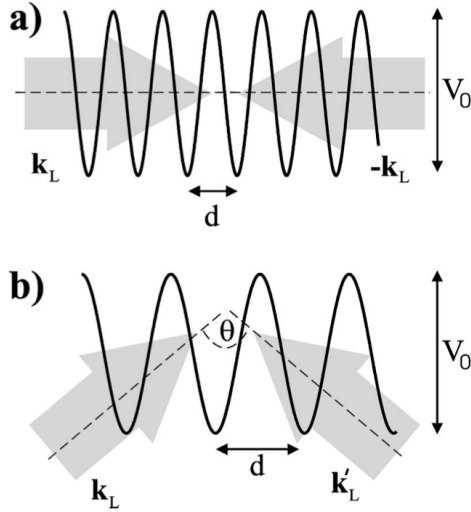


Figure 2.5: A one-dimensional optical lattice created from (a) counter propagating laser beams and (b) with beams enclosing an angle. The parameters lattice depth and lattice spacing are defined in the text. Figure taken from [37].

higher energy state, also needs to be taken into account and avoided. The spontaneous scattering rate of atoms at the center of a trap is proportional to $\frac{I_p}{\Delta^2}$ [37]. Thus, a large detuning will cause the spontaneous scattering to be negligible in comparison to the depth of the lattice sites.

The potential created by two interfering lasers with a wavelength λ_L is [37]

$$V(x) = V_0 \cos^2 \left(\frac{2\pi x}{\lambda_L} \right) \quad (2.4)$$

where $\lambda_L/2$ is the distance d between the two minima in the direction of the laser beam. This relationship is illustrated in Fig. 2.5. So, the depth of the wells can be adjusted by placing two counter propagating laser beams opposite to one another as shown in Fig. 2.5a or by adjusting a phase difference between the two lasers by changing θ as in Fig. 2.5b. Therefore, we can control the potential depth in addition to the detuning, allowing us to minimize both the photon-particle and the particle-particle interactions which would excite the system out of the ground state.

2.3 Bose-Hubbard Hamiltonian

The simplest non-trivial model that describes interacting bosons on a lattice of s wells or sites, is the Bose-Hubbard Hamiltonian (BHH). Due to the low density of the gas needed to achieve a BEC, the number of three-body collisions is negligible, allowing us to consider only two-body scattering events, which can be described sufficiently by s -wave scattering due to the low energies of the involved particles [15]:

$$\hat{H} = \sum_{i=1}^s \varepsilon_i \hat{n}_i + \frac{1}{2} \sum_{i=1}^s U_i \hat{n}_i (\hat{n}_i - 1) - \frac{1}{2} \sum_{i,j}^s k_{i,j} [\hat{b}_i^\dagger \hat{b}_j + \hat{b}_j^\dagger \hat{b}_i], \quad (2.5)$$

where ε_i is the onsite potential at each site i and $k_{i,j}$ is the tunneling rate between adjacent sites i and j . The operators $\hat{n}_i = \hat{b}_i^\dagger \hat{b}_i$ count the number of bosons at site i . The annihilation and creation operators, \hat{b}_i and \hat{b}_i^\dagger , obey the commutation relations $[\hat{b}_i, \hat{b}_j^\dagger] = \delta_{i,j}$. The onsite interaction strength is represented by U_i , which, due to the low temperatures necessary to achieve a Bose-Einstein condensate, is governed predominantly by s -wave scattering. The Hamiltonian, Eq. (2.5), has two constants of motion: the energy E and the total number of particles $N = \sum_{i=1}^s n_i$. The interaction potential is often approximated as a delta function due to the inherent low particle density of the BEC [32]. In this approximation, the interatomic interaction strength is equal to

$$U_i = \frac{4\pi a_s \hbar^2}{m} \quad (2.6)$$

where a_s is the s -wave scattering and m is the mass of the particles.

Experimentally, all three parameters, ε , U , and k can be controlled. For example, in optical lattices, the onsite potential is directly related to the intensity of the lasers used to create the lattice potential [32]. The interaction strength can be modified by changing a_s . The s -wave scattering length can be adjusted to both negative and positive values by applying an external magnetic, optical, radio-frequency, or electric field [48]. Finally, the tunneling rate can be regulated by changing the depth of the lattice sites [32].

2.3.1 The BHH in Fock-space

The wavefunction associated with bosons trapped in a lattice potential is most easily represented in Fock-space. The total number of particles N is

$$N = \sum_{i=1}^s n_i. \quad (2.7)$$

N is a constant of motion, both in the quantum and classical limits. This can be seen for the quantum case by calculating the commutation relation between the BHH [Eq. (2.5)] and the total number of particles [Eq. (2.7)]. Specifically, we find

$$\frac{\partial N}{\partial t} = \frac{i}{\hbar} \langle [\hat{H}, N] \rangle = 0. \quad (2.8)$$

In the classical limit, the Poisson bracket of the classical Hamiltonian [Eq. (2.15)] and the total number particles is $\frac{\partial N}{\partial t} = \{\mathcal{H}, N\} = 0$. Hence, in the classical limit, the total number of particles in the system is also conserved.

By using the Fock number states, $|n_1, n_2, \dots, n_i, \dots, n_s\rangle$, as a basis, we can easily describe the number of atoms, n_i , at each site using any of the vectors spanned in the Fock-space

$$\left\{ \underbrace{|N, 0, \dots, 0\rangle}_{s \text{ terms}}, |N-1, 1, \dots, 0\rangle, |N-1, 0, 1, 0, \dots, 0\rangle, \dots, |N-1, 0, \dots, 0, 1\rangle, |N-2, 2, 0, \dots, 0\rangle, \right. \\ \left. |N-2, 1, 1, 0, \dots, 0\rangle, \dots, |N-2, 0, \dots, 2\rangle, \dots, |0, \dots, 0, N\rangle \right\} \quad (2.9)$$

The raising and lowering operators act as such on the wavefunctions:

$$\hat{b}_i |n_1, n_2, \dots, n_i, \dots, n_s\rangle = \sqrt{n_i} |n_1, n_2, \dots, n_i - 1, \dots, n_s\rangle \quad (2.10)$$

$$\hat{b}_i^\dagger |n_1, n_2, \dots, n_i, \dots, n_s\rangle = \sqrt{n_i + 1} |n_1, n_2, \dots, n_i + 1, \dots, n_s\rangle \quad (2.11)$$

One can then use this basis in order to write the BHH [Eq. (2.5)]. The dimension of

our Hilbert space \mathcal{N} is defined by the number of different ways our N indistinguishable bosons can be distributed among the s different wells [4]

$$\mathcal{N} = \frac{(N + s - 1)!}{N!(s - 1)!}. \quad (2.12)$$

2.4 The Classical Limit of the BHH and the Discrete Nonlinear Schrödinger Equation

Interacting bosonic systems described by the BHH have a well-defined classical limit and these provide excellent models with which fundamental issues concerning quantum-classical correspondence (QCC) can be investigated, both theoretically and experimentally. Below we describe a method that will allow us to identify the classical limit of the BHH. To this end, we define new raising and lowering operators:

$$\hat{A}_i = \frac{1}{\sqrt{N}} \hat{b}_i; \quad \hat{A}_i^\dagger = \frac{1}{\sqrt{N}} \hat{b}_i^\dagger; \quad \hat{n}_i = \frac{1}{N} \hat{n}_i \quad (2.13)$$

With these new raising and lowering operators the BHH becomes

$$\frac{\hat{H}}{N} = \sum_{i=1}^s \varepsilon_i \hat{n}_i + \frac{N}{2} \sum_{i=1}^s U_i \hat{n}_i (\hat{n}_i - \frac{1}{N}) - \frac{1}{2} \sum_{\langle i,j \rangle} k_{i,j} [\hat{A}_i^\dagger \hat{A}_j + \hat{A}_j^\dagger \hat{A}_i], \quad (2.14)$$

which is the energy per boson.

Assuming that the lattice is homogenous, i.e. the interatomic interactions and the tunneling rates are the same for all sites ($U_i = U$ and $k_{i,j} = k$), we rewrite Eq. (2.14) such that UN stays constant as N is changed. Now when we take the limit $N \rightarrow \infty$, our new Hamiltonian is

$$\mathcal{H} = \frac{\hat{H}}{N} = \sum_{i=1}^s \varepsilon_i \hat{n}_i + \frac{\tilde{U}}{2} \sum_{i=1}^s \hat{n}_i \hat{n}_i - \frac{k}{2} \sum_{\langle i,j \rangle} [\hat{A}_i^\dagger \hat{A}_j + \hat{A}_j^\dagger \hat{A}_i], \quad (2.15)$$

2 Cold Bosons Interacting on a Lattice

in which we have introduced the effective nonlinearity

$$\tilde{U} = UN. \quad (2.16)$$

Next, we note that the commutation relation between \hat{A}_i and \hat{A}_i^\dagger goes to zero for large N , since

$$[\hat{A}_i, \hat{A}_j^\dagger] = \frac{1}{N} \delta_{i,j}. \quad (2.17)$$

In fact, from Eq. (2.17), we can define an effective $\hbar_{eff} = 1/N$. Additionally, we note that since, in the limit $N \rightarrow \infty$, the right-hand side of Eq. (2.17) goes to zero, \hat{A}_i and \hat{A}_i^\dagger become c-numbers. In this classical limit, the quantum Hamiltonian [Eq. (2.15)] transforms into its classical counterpart:

$$\mathcal{H} = \sum_{i=1}^s \varepsilon_i |A_i|^2 + \frac{\tilde{U}}{2} \sum_{i=1}^s |A_i|^4 - \frac{k}{2} \sum_i [A_i^* A_{i-1} + A_{i-1}^* A_i]. \quad (2.18)$$

The Hamiltonian, Eq. (2.18), describes a system of s nonlinear coupled oscillators. The generated dynamics is determined by the dimensionless ratio $u = NU/k$: For $u \rightarrow \infty$ the interaction term dominates and the system behaves as a set of uncoupled oscillators while for $u \rightarrow 0$ the kinetic term dominates. In both extremes, the classical dynamics is integrable. For intermediate values of u (and for $s > 2$) chaotic motion emerges. We thus conclude that the appropriate semiclassical limit is $N \rightarrow \infty$ (i.e. $\hbar_{eff} \rightarrow 0$), while simultaneously keeping \tilde{U} constant such that the underlying classical dynamics remains unchanged. The amplitudes A_i and A_i^* are conjugate variables with respect to the Hamiltonian, $i\mathcal{H}$. The resulting canonical equations of motion read:

$$i \frac{\partial A_l}{\partial t} = \frac{\partial \mathcal{H}}{\partial A_l^*}; \quad -i \frac{\partial A_l^*}{\partial t} = \frac{\partial \mathcal{H}}{\partial A_l}, \quad (2.19)$$

from which we can derive the Discrete Nonlinear Schrödinger (DNLS) equation

$$i \dot{A}_l = \varepsilon_l A_l + \tilde{U} |A_l|^2 A_l - \frac{k}{2} (A_{l-1} + A_{l+1}). \quad (2.20)$$

2 Cold Bosons Interacting on a Lattice

The DNLS equation will allow us to solve for A_l associated with the lattice potential, therefore providing a means to compare and contrast the quantum and classical observables for the system.

2.5 Bose-Hubbard Dimer

For a two site lattice, the BHH Eq. (2.5) becomes

$$\hat{H} = \varepsilon_1 \hat{n}_1 + \varepsilon_2 \hat{n}_2 + \frac{U_1}{2} \hat{n}_1(\hat{n}_1 - 1) + \frac{U_2}{2} \hat{n}_2(\hat{n}_2 - 1) - \frac{k}{2} (\hat{b}_1^\dagger \hat{b}_2 + \hat{b}_2^\dagger \hat{b}_1) \quad (2.21)$$

where, for sake of simplicity, we have relabeled k_{12} as k .

In order to do numerical calculations of the state vectors for the quantum BHH, we need to derive the matrix form of the Hamiltonian. The Fock state for the dimer $|n_1, n_2\rangle$ can be rewritten via $n_1 + n_2 = N$ as $|n, N - n\rangle \equiv |n\rangle$. To calculate the matrix for of the BHH, we sandwich Eq. (2.21) between two different state vectors, $\langle m | \hat{H} | n \rangle$ where $m, n \in \mathbb{Z}$ and run from 1 to $\mathcal{N} = N + 1$. For the dimer, the Hamiltonian matrix in the Fock space reads:

$$\begin{aligned} \langle m | \hat{H} | n \rangle = & [\varepsilon_1 n + \varepsilon_2 (N - n) + \frac{U_1}{2} n(n - 1) + \frac{U_2}{2} (N - n)(N - n - 1)] \delta_{n,m} \\ & - \frac{k}{2} \sqrt{n(N - n + 1)} \delta_{n,m+1} - \frac{k}{2} \sqrt{(n - N)(n + 1)} \delta_{n,m-1} \end{aligned} \quad (2.22)$$

In Fig. 2.6, based on Ref. [26], the calculations for the energy levels of a system of twenty-nine particles is shown. In the limit of small coupling strength, the energy levels are doubly degenerate. As the coupling strength is increased, the degeneracy is lifted, beginning from the lower energy levels until the levels bifurcate into \mathcal{N} energy levels.

The dimer model has been studied both theoretically and experimentally. One example of experimental work will be discussed in the next section.

2 Cold Bosons Interacting on a Lattice

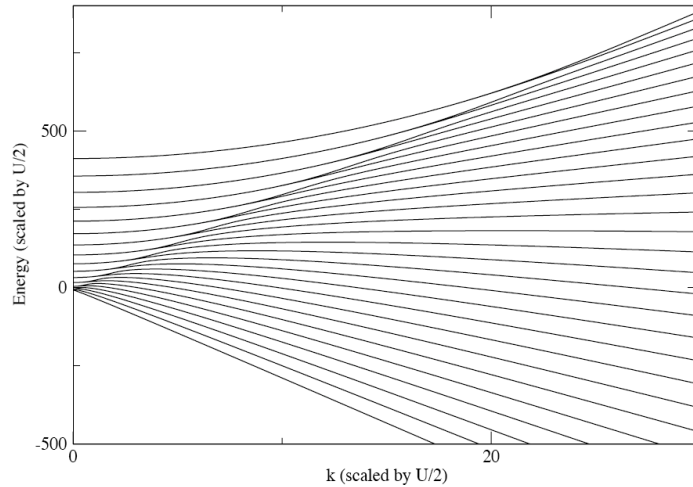


Figure 2.6: The energies obtained for the Bose-Einstein condensate in a double well potential. The onsite potentials $\varepsilon_i = 0$, the interatomic interaction strengths $U_1 = U_2 = U$, and $N = 29$. For small k the energy levels come in degenerate pairs. As the coupling strength is increased, the energy levels, beginning with the lowest, begin to break their degeneracy.

2.6 The Heidelberg Experiment

One of the first, and most fundamental, textbook examples highlighting the differences between quantum and classical mechanics is the tunneling of a quantum particle through a potential barrier. It demonstrates the manifestation of the wave nature of matter. Experimentally, such processes can be studied on a mesoscopic level. A variety of experiments have been done on this topic. The most relevant experiment to our research is the recent work of the Heidelberg group on the Josephson effect between two weakly coupled atomic Bose-Einstein condensates in a macroscopic double well potential[1].

Although Josephson junctions have been realized in other experimental set-ups, such as superconductors separated by a thin insulator [33] or in super fluid helium stored in two reservoirs connected by nanoscopic apertures [40, 50], Oberthaler's system was the first in which the nonlinear interatomic interactions played an essential role in the dynamics. The nonlinearity revealed new dynamical behaviors: when the atom popula-

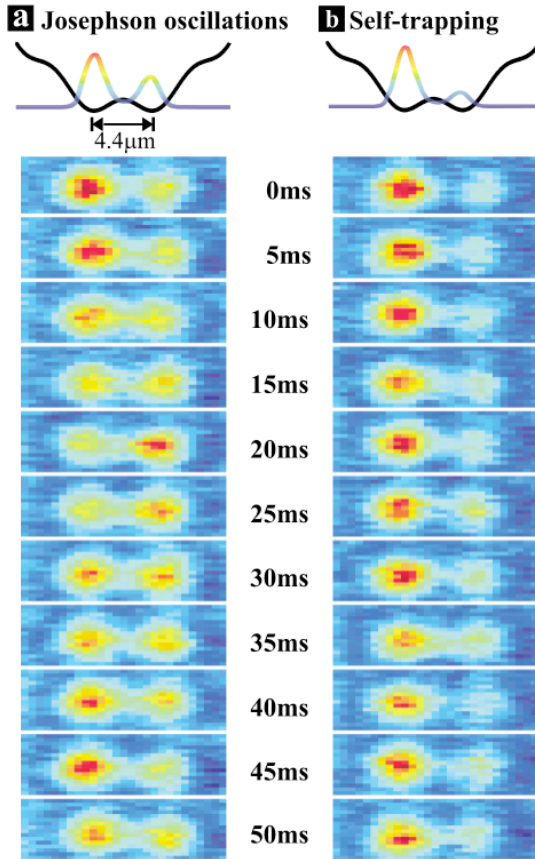


Figure 2.7: Observation of tunneling dynamics of two weakly linked Bose-Einstein condensates in a symmetric double well potential as indicated in the schematics. The time evolution of the population of the left and right potential well is directly visible in the absorption images ($19.4 \mu\text{m}$ $10.2 \mu\text{m}$). The distance between the two wavepackets is increased to $6.7 \mu\text{m}$ for imaging. (a) Josephson oscillations are observed when the initial population difference is chosen to be below the critical value z_c . (b) In the case of an initial population difference greater than the critical value the population in the potential minima is nearly stationary. This phenomenon is known as macroscopic quantum self-trapping. Figure taken from [38].

tion imbalance between the two wells was below a critical value, Josephson oscillations were predicted and observed, as in Fig. 2.7a; while when the population imbalance was above the critical value, the Josephson oscillations were hindered, and thus self-trapping behavior was predicted and observed, as shown in Fig. 2.7b.

In this experiment the Heidelberg group used a ^{87}Rb BEC. Laser cooling techniques as discussed in §2.2 were used with 811 nm wavelength lasers to achieve a BEC of 1150 ± 150 atoms in a double well potential with final trap frequencies of $\omega_x = 2\pi \times 90(1)\text{Hz}$, $\omega_y = 2\pi \times 66(1)\text{Hz}$, and $\omega_z = 2\pi \times 90(1)\text{Hz}$ (which give the harmonic oscillation frequency of an atom trapped inside the lattice well). Gravity is acting in the y -direction. The lasers were then adjusted to increase the depth of the wells in the x -direction to $2\pi \times 412(20)\text{Hz}$. They were crossed at a relative angle of 9° so that their interference pattern would create a periodic potential with strong harmonic confinement, thus producing an effective

2 Cold Bosons Interacting on a Lattice

double well potential with a barrier height of $2\pi \times 263(20)Hz$ and a separation of $4.4(2) \mu\text{m}$ as in Fig. 2.7.

The initial preparation of the population imbalance is achieved by shifting the relative angle of the laser via a piezo actuated mirror mount to create an asymmetrical potential. The BEC is then loaded into the asymmetrical double well and the laser is adjusted to recreate a symmetrical potential. Since the BEC will seek the lowest possible energy, the larger the degree of asymmetry of the double well, the higher the population will be in the lower well. Thus, a greater degree of asymmetry is used to achieve self-trapping than to realize Josephson oscillations (see top frames of Fig. 2.7). To initiate Josephson oscillations, the asymmetrical double well is nonadiabatically converted to a symmetrical double well potential, so that the dynamics does not begin before the double well has been symmetrized. The self-trapping regime does not necessitate such a fast transformation of the potential, since its states evolve very slowly. Thus, it was possible to create any initial population difference with a standard deviation of 0.06. In the Josephson Junction (JJ) regime, the small inter-well separation allows particles to achieve a tunneling time on the order of 40 ms (as can be seen in Fig.2.7a). This must be contrasted with the tunneling time of past realizations of BECs in double well potentials [51, 44], which is on the order of thousands of seconds. As a consequence of the shorter time scale, Oberthaler and his group were the first to make direct observations of the nonlinear dynamics in a single bosonic Josephson junction. Furthermore, it is important to note that the tunneling time of 40 ms observed in the ^{87}Rb Bose-Einstein condensate in the JJ regime is much shorter than the tunneling time of 500 ms observed in the same system for noninteracting particles [1]. This observation, together with the appearance of the self-trapping phenomenon observed by the Heidelberg group, clearly indicates the importance of interatomic interactions in the tunneling process.

3 Dynamics of the Symmetric Dimer

This chapter is dedicated to investigating the Fock space wavepacket dynamics of a BEC trapped in a deep double well potential. To this end, we will employ time-dependent perturbation theory for small tunneling rates between the two wells and note three important frequencies which determine the behavior of the system. We then analyze the corresponding classical phase space. The mean-field approach allows us to distinguish three regimes: Josephson oscillations (large coupling), the self-trapping regime (small couplings), and the intermediate regime where the dynamics is dictated by a stretching mechanism imposed by a separatrix in the phase-space. We simultaneously demonstrate that the classical methods are unable to accurately describe the quantum dynamics on long time scales. In the final part of the chapter we explore the strength of semiclassical considerations, showing that semiclassics can capture the essential features of the quantum dynamics in all three dynamical regimes: Josephson oscillations, self-trapping, and the transition regime. We go a step further than the existing literature in this section, as our approach captures not only the temporal behavior of the mean atomic population, but is actually capable of describing the whole evolving occupation statistics accurately.

3.1 Wavepacket Dynamics: Quantum Calculations

We first want to explore the quantum time evolution of the atomic population imbalance. To this end we numerically integrate the time-dependent Schrödinger equation associated with the Hamiltonian, Eq. (3.1), of the dimer. The evolving state is $|\psi(t)\rangle$ and we are interested in the evolving occupation distribution $P_n(t) = |\psi_n(t)|^2$ where

3 Dynamics of the Symmetric Dimer

the occupation probability amplitude is defined as $\psi_n(t) = \langle n | \psi(t) \rangle$. As stated in §2.5, $|n\rangle \equiv |n, N - n\rangle = |n_1, n_2\rangle$. We will discuss the case in which all the bosons initially occupy one of the two wells, i.e. $n_1(t = 0) = N$ and $n_2(t = 0) = 0$. The corresponding wavefunction in the Fock space is $|\psi_0\rangle \equiv |\psi(t = 0)\rangle \equiv |N, 0\rangle$.

Now we would like to explore the dynamical scenarios which can be generated by the Schrödinger equation for $\psi_n(t)$. Namely,

$$i\hbar \frac{d\psi_n(t)}{dt} = H_{n,n}\psi_n(t) + H_{n,n+1}\psi_{n+1}(t) + H_{n,n-1}\psi_{n-1}(t), \quad (3.1)$$

where $H_{n,m}$ is given in the Fock basis by Eq. (2.22). We describe the occupation profile for $t > 0$ by the probability distribution, or occupation statistics, $P_n(t)$. In particular, it is convenient to characterize the spreading profile using the various moments q of the population imbalance operator $\langle \psi(t) | (b_1^\dagger b_1 - b_2^\dagger b_2)^q | \psi(t) \rangle$. The literature thus far takes a special interest in the study of the first moment of the population imbalance operator [26, 27, 28].

We can explore the occupation statistics of our system for various values of the interatomic interaction U and the coupling constant k . Two of these limits are the small coupling regime ($k \ll U$) and the small interatomic interaction regime ($U \ll k$). In both of these extremes, we can study the behavior of the system using perturbation theory.¹

The dynamics of the small coupling limit is shown in Fig. 3.1. We report our numerical results for the expectation value (i.e. first moment) of the normalized population imbalance $(n_1 - n_2)/N$ in a system of 10 bosons. One can clearly recognize the appearance of various time scales in the evolution [27]. For short times, the amplitude of the oscillations about the initial preparation is very small (see top panel of Fig. 3.1), which tracks with the work done in Oberthaler's group (Fig. 2.7). However, as we move into longer times scales, such as the middle panel of Fig. 3.1, we see that, though the bosons remain localized, the quantum dynamics differ from the results reported by the

¹For a more detailed exploration of our work on the perturbation theory, please refer to Ref [46]

3 Dynamics of the Symmetric Dimer

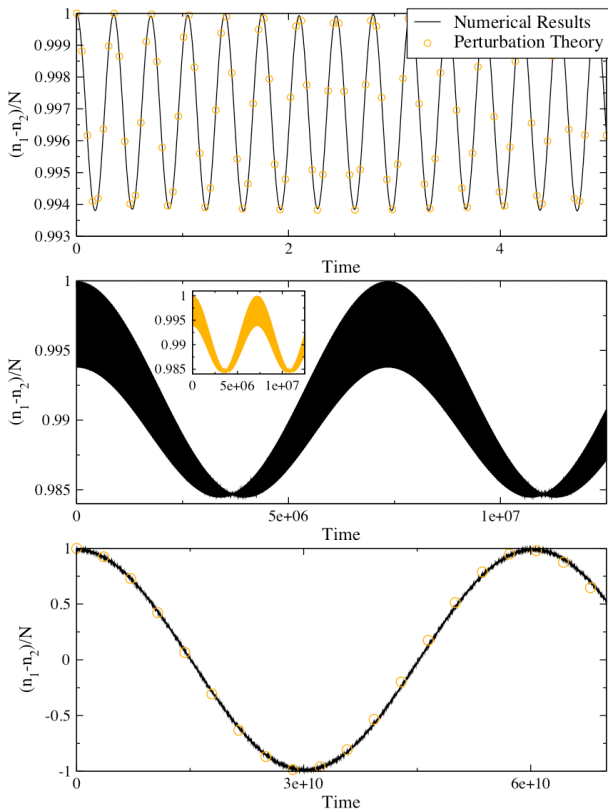


Figure 3.1: The time evolution for various time scales of a dimer system with $N = 10$, $k = 1$, and $\tilde{U} = 1$, based on Ref. [27]. Note that though on short time scales, the localized state stays trapped, on long time scales, tunneling allows the bosons to move from one well to the other, thus causing the states to oscillate between $|N, 0\rangle$ and $|0, N\rangle$. The numerical results are in black, while the analytical results are in orange. Note that there is good agreement between the numerical and analytical results.

Heidelberg group. As was shown in Ref. [27], a secondary frequency begins to affect the dynamics at this time scale, resulting, in conjunction with the high frequency of the short time scale, in a beating that causes collapses and growths in the amplitude of the population imbalance. This beat is a result of the splitting of the second highest quasi-degenerate pair of energy levels. Finally, at very large time scales (see the bottom panel of Fig. 3.1), we find that the bosons tunnel coherently between the two wells, i.e. from state $|N, 0\rangle$ to $|0, N\rangle$ and back, a phenomenon not captured by the Heidelberg group at all. This behavior is due to the fact that $|N, 0\rangle$ and $|0, N\rangle$ are not eigenstates of the system. As a result, the initial preparation has to decompose into the symmetric and antisymmetric combinations of localized states at each trap. The lifting of the degeneracy of the higher-lying energy levels provides the corresponding tunneling frequency [27].

In Ref. [27], using N th order time-dependent perturbation theory, the normalized

3 Dynamics of the Symmetric Dimer

population imbalance was found to be:

$$\frac{n_1 - n_2}{N} = - \left(\cos(\omega_0 t) + \frac{k^2}{8U^2(N-1)^2} \left[\frac{N}{2} [\cos(\omega_1 t) - \cos(\omega_0 t)] + 2\cos(\omega_\mu t)\cos\left(\frac{\omega_1}{2}t\right) - \cos(\omega_1 t) - \cos(\omega_0 t) \right] \right) \quad (3.2)$$

The frequencies

$$\omega_\mu = \frac{U}{2} \left[2(N-1) - \left(\frac{k}{U}\right)^2 \frac{N+1}{N^2 - 4N + 3} \right], \quad (3.3)$$

$$\omega_1 = \frac{U}{2} \left[\left(\frac{k}{U}\right)^{N-2} \frac{(N-1)(N-2)}{2^{N-4}(N-3)!} \right], \quad (3.4)$$

$$\omega_0 = \frac{U}{2} \left[\left(\frac{k}{U}\right)^N \frac{N}{2^{N-1}(N-1)!} \right]. \quad (3.5)$$

are found by 1st, $(N-1)$ th, and N th order perturbation theory, respectively. The frequency ω_μ represents the difference between the highest energy levels (all bosons on site 1 or all on site 2) and the second highest energy levels ($|N-1, 1\rangle$ or $|1, N-1\rangle$). It models the population imbalance for short times, as seen in the upper subfigure of Fig. 3.1. The splitting of the second highest energy levels corresponds to ω_1 , which, in conjunction with ω_μ creates the beat in the middle subfigure of Fig. 3.1. Finally, the frequency ω_0 corresponds to the splitting between the highest energy levels ($|N, 0\rangle$ and $|0, N\rangle$). We also dub this frequency k_{eff} , a quantity which will be utilized in Chapter 5, since it determines the movement of the entire cloud of bosons from one site to the other. Influence of the effective tunneling rate k_{eff} can be seen in the third subfigure of Fig. 3.1.

After studying the small coupling limit, we turned to the other extreme, the small interatomic interaction regime. We found an expression for all moments of the population imbalance to first order. The results of this work can be seen in Fig. 3.2. As in the small coupling limit, higher orders would allow us to better match the dynamics of the system using perturbation theory. However, the complexity of the equations which appear in

3 Dynamics of the Symmetric Dimer

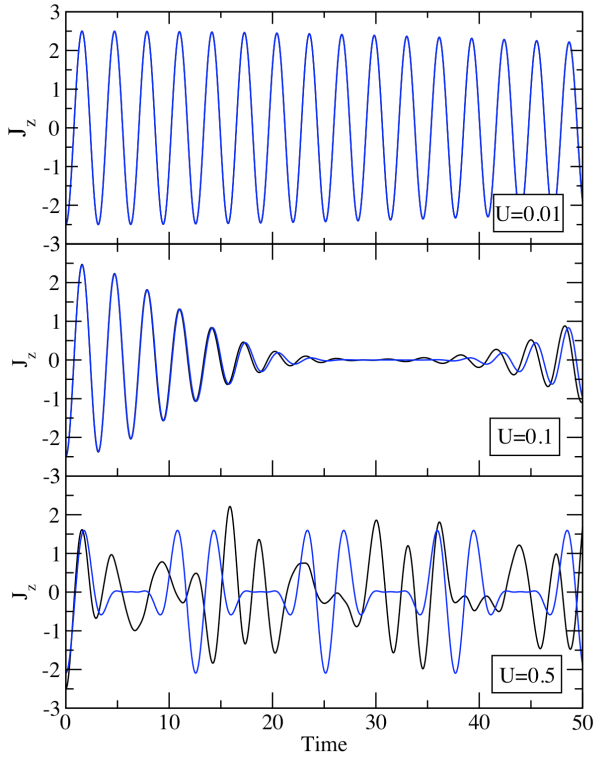


Figure 3.2: The first moment of $\langle J_z \rangle = \langle (b_1^\dagger b_1 - b_2^\dagger b_2)/2 \rangle$ for different interatomic interactions, where $k = 2$ and $N = 5$. The black line was produced by quantum numerics. The blue line is the first order perturbation theory (see Ref. [46]).

small interatomic interaction perturbation theory [46], makes exploring other analytical methods, such as the classical analysis discussed in the next section, appealing.

3.2 Dimer in SU(2) Formalism

Without loss of generality, we can assume an even $N \gg 1$. We can rewrite the BHH, Eq. (2.21), in the angular momentum representation or SU(2) formalism. To this end, we define the following three operators, which obey SU(2) commutation relations

$$\hat{J}_x = \frac{1}{2} (\hat{b}_1^\dagger \hat{b}_2 + \hat{b}_2^\dagger \hat{b}_1), \quad \hat{J}_y = \frac{i}{2} (\hat{b}_1^\dagger \hat{b}_2 - \hat{b}_2^\dagger \hat{b}_1), \quad \hat{J}_z = \frac{1}{2} (\hat{b}_1^\dagger \hat{b}_1 - \hat{b}_2^\dagger \hat{b}_2). \quad (3.6)$$

The angular momentum operator \hat{J}_x corresponds to the coupling term in the BHH, and \hat{J}_z corresponds to the population imbalance between the two wells. The Casimir

3 Dynamics of the Symmetric Dimer

invariant is trivially found to be

$$J^2 = \frac{N}{2} \left(\frac{N}{2} + 1 \right). \quad (3.7)$$

This is analogous to an angular momentum model in which the total angular momentum is given by $j = N/2$. At this point, we also introduce $\varepsilon = \varepsilon_2 - \varepsilon_1$, which is the bias between the onsite potentials. Plugging this into the BHH, we can rewrite it as

$$\hat{H} = U \hat{J}_z^2 - \varepsilon \hat{J}_z - k \hat{J}_x + \frac{N}{2}(\varepsilon_2 + \varepsilon_1) + \frac{U}{2} \left(\frac{N^2}{2} - N \right) \quad (3.8)$$

The constant term $N(\varepsilon_2 + \varepsilon_1)/2 + U(N^2/2 - N)/2$ does not contribute to the dynamics of the system and thus will be ignored.

The dynamics of the system for finite interatomic interaction U is more conveniently analyzed if we rewrite Eq. (3.8) with canonically conjugate variables. In this situation we are formally looking at the dynamics of two coupled oscillators, allowing us to define action-angle variables $\hat{b}_j = \sqrt{\hat{n}_j} e^{i\hat{\varphi}_j}$. By denoting the population imbalance $\hat{n} = \hat{J}_z$ and the relative phase $\hat{\varphi} = \hat{\varphi}_1 - \hat{\varphi}_2$, Eq. (3.8) can be rewritten as

$$\hat{H} = U \hat{n}^2 - \varepsilon \hat{n} - \frac{k}{2} \left[\sqrt{\left(\frac{N}{2} - \hat{n} \right) \left(\frac{N}{2} + \hat{n} + 1 \right)} e^{-i\hat{\varphi}} + \sqrt{\left(\frac{N}{2} + \hat{n} \right) \left(\frac{N}{2} - \hat{n} + 1 \right)} e^{i\hat{\varphi}} \right]. \quad (3.9)$$

In the limit $N \gg 1$, we can consider that $N + 2 \approx N$; thus the Hamiltonian becomes

$$\hat{H} \approx U \hat{n}^2 - \varepsilon \hat{n} - k \sqrt{\left(\frac{N}{2} - \hat{n} \right) \left(\frac{N}{2} + \hat{n} \right)} \cos \hat{\varphi} = U \hat{n}^2 - \varepsilon \hat{n} - k \sqrt{\left(\left(\frac{N}{2} \right)^2 - \hat{n}^2 \right)} \cos \hat{\varphi}. \quad (3.10)$$

As we are working in SU(2) formalism, we would like to be able to visualize our phase space topology on the Bloch sphere. The current form of the Hamiltonian, Eq. (3.10), does not lend itself well to visualizing the global topology of the phase space, but we can define an additional variable $\hat{\theta}$ such that $\hat{J}_z = \hat{n} = \frac{N}{2} \cos \hat{\theta}$, while $\hat{J}_x \approx \frac{N}{2} \sin \hat{\theta} \cos \hat{\varphi}$.

3 Dynamics of the Symmetric Dimer

Note that $\hat{\theta}$ and $\hat{\varphi}$ do not commute. In these coordinates, the Hamiltonian becomes

$$H \approx \frac{Nk}{2} \left[\frac{u}{2} \cos^2 \hat{\theta} - \frac{\varepsilon}{k} \cos \hat{\theta} - \sin \hat{\theta} \cos \hat{\varphi} \right] \quad (3.11)$$

where we have defined the scaled parameter $u = \frac{NU}{k}$.

3.3 Classical Considerations

We begin our analysis by investigating the structure of the underlying classical phase space of the system. First we rewrite Eq. (3.11) in terms of the fractional population difference $S_z = \frac{J_z}{N/2} = \frac{n_1 - n_2}{N}$

$$H \approx \frac{Nk}{2} \left[\frac{u}{2} S_z^2 - \frac{\varepsilon}{k} S_z - \sqrt{1 - S_z^2} \cos \varphi \right]. \quad (3.12)$$

Hamilton's equations can then be written in terms of the spatial and momentum coordinates φ and S_z

$$\dot{\varphi} = \frac{dH}{dS_z}; \quad \dot{S}_z = -\frac{dH}{d\varphi}. \quad (3.13)$$

Thus, the classical equations of motion are [45]

$$\dot{S}_z = -\sqrt{1 - S_z^2} \sin \varphi \quad (3.14)$$

$$\dot{\varphi} = u S_z - \frac{\varepsilon}{k} + \frac{S_z}{\sqrt{1 - S_z^2}} \cos \varphi. \quad (3.15)$$

These equations of motion allow us to compare the classical evolution of the system to the quantum results as shown in Fig. 3.3. Note that the classical calculations capture the frequencies of the self-trapped and Josephson oscillation regimes, but not their amplitude decay. The correspondence in the transition between the two regimes in the transition between the two regimes, on the other hand, breaks down very quickly.

3 Dynamics of the Symmetric Dimer

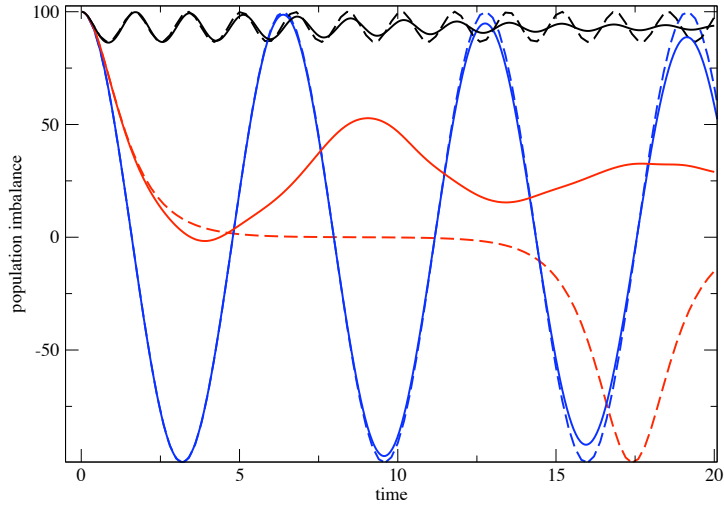


Figure 3.3: The quantum (solid lines) and classical (dashed lines) results for the population imbalance in three regimes. The Josephson oscillation regime ($u = 0.5$) is shown in blue, while the self-trapping regime ($u = 4$) is shown in black. The transition between the the Josephson oscillation and self-trapping regimes is shown in red ($u = 2$).

3.3.1 Analysis of the Phase Space

We can describe the phase space of our system in multiple ways. One is using the canonical coordinates (φ, n) , so that the total area of the phase space is $2\pi N$ and the Planck cell is given by $2\pi\hbar$. Another is using normalized coordinates $(\varphi, \cos\theta)$, where the total phase space area is 4π and the Planck cell is $4\pi/N$. We can visualize either of these representations on the Bloch sphere. While it can be useful to visualize three dimensional representation of the Bloch sphere, it is convenient to use (X, Z) (or EAST-WEST) images of the spherical phase space (see Fig. 3.4), since it allows us to see the topology from two angles. The (X, Z) images use the definitions

$$Z = \cos(\theta) \tag{3.16a}$$

$$X = \sin(\theta) * \varphi \quad \text{for } |\varphi| < \pi/2 \tag{3.16b}$$

$$X = \sin(\theta) * (\varphi - \pi) + \pi \quad \text{for } |\varphi - \pi| < \pi/2 \tag{3.16c}$$

3 Dynamics of the Symmetric Dimer

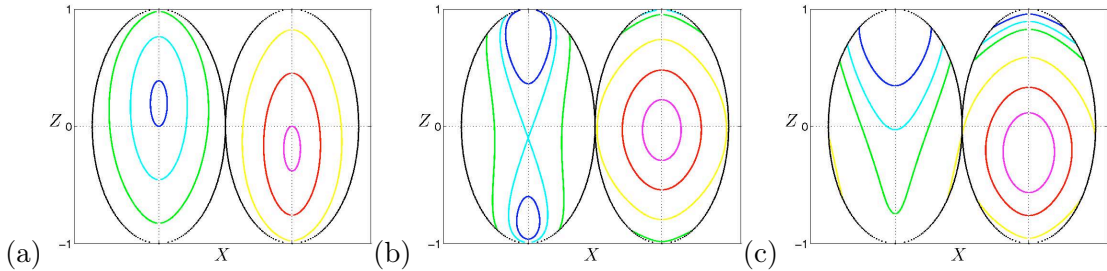


Figure 3.4: The (X, Z) images showing the contour lines of constant energy in phase space. The view on the left of (a), (b), and (c) is the "WEST" perspective, while on the right is the "EAST" perspective. (a) corresponds to $u \ll 1$, where the dynamics is controlled by the $\sin \theta$ term of Eq. (3.17) and there are only two fixed points. (b) corresponds to $u \sim 1$ and $|\varepsilon| < \varepsilon_c$, where we see two maxima and a saddle point on the WEST side and a minimum on the EAST side. Finally, (c) shows the phase space for $u > 1$ and $|\varepsilon| > \varepsilon_c$.

The bias ε and the scaled parameter u determine the topology of the phase space. We could approach studying the energy contours by doing 2D contour plots, showing how the energy Eq. (3.11) depends on both φ and θ ; however, as can be readily seen in Fig. 3.4b, the interesting behavior in the phase space occurs at $\varphi = 0$. Thus, to study the extrema of the energy, we can focus on this section, writing the energy as

$$E(\theta) \propto \frac{1}{2}u \cos^2 \theta - \frac{\varepsilon}{k} \cos \theta - \sin \theta. \quad (3.17)$$

We can find the fixed points in phase space via its derivative

$$E'(\theta) = \frac{1}{2}u \sin(2\theta) + \frac{\varepsilon}{k} \sin \theta - \cos \theta = 0. \quad (3.18)$$

The number of solutions to Eq. (3.18) depends on u and ε . There are two fixed points when $u < 1$ (see Fig. 3.4a). If $u > 1$, there are two cases: (i) there are two fixed points when $|\varepsilon| \geq \varepsilon_c$ and (ii) four fixed points when $|\varepsilon| < \varepsilon_c$ (as shown in Fig. 3.4b and c, respectively). The critical bias which determines these fixed points is obtained

3 Dynamics of the Symmetric Dimer

by solving the equations $E'(\hat{\theta}) = 0$ and $E''(\hat{\theta}) = 0$ simultaneously (see Appendix A):

$$\varepsilon_c = k \left(u^{2/3} - 1 \right)^{3/2} \quad (3.19)$$

As can be seen in Fig. 3.4b, when $|\varepsilon| < \varepsilon_c$ a separatrix divides the phase space into what we dub two islands (the maxima on the WEST side) and a sea. When $\varepsilon = 0$, we can calculate the fixed points analytically:

$$\hat{\theta}_O = \pi/2 \quad (3.20a)$$

$$\hat{\theta}_X = -\pi/2 \quad (3.20b)$$

$$\hat{\theta}_{1,2} = -\arcsin(1/u) \quad (3.20c)$$

From Fig. 3.4b, it is clear that the separatrix which encloses the $\hat{\theta}_{1,2}$ islands has a figure eight shape. When $\varepsilon = 0$, this separatrix is symmetric. For $\varepsilon_c > |\varepsilon| \neq 0$, the separatrix has an asymmetric shape, in which one of the islands is smaller than the other. In the case that $|\varepsilon| \sim \varepsilon_c$, the separatrix no longer has a figure eight shape, as one of the islands has vanished completely, while the other has a phase space area A_c . This critical phase space area is the action and can be found to be [47, 34]

$$A_c \approx \frac{4\pi\varepsilon_c}{ku}. \quad (3.21)$$

Via the standard Bohr-Sommerfeld quantization relation $A_c = n_c \hbar_{eff}$, we can calculate the index of the energy contour which falls closest to the separatrix in our phase space. The index is

$$n_c \approx \left(1 - u^{-2/3} \right)^{3/2} N. \quad (3.22)$$

3.4 Characteristic Frequencies of the Classical Dynamics

In the case of the symmetric double well (where $\varepsilon = 0$), we can isolate the effect of u on the system. Its effect can be seen most readily in the phase space of the system on the Bloch sphere (see Fig. 3.4). We can use this u to define a few different regimes. If $u = 0$, then all the trajectories of the system have the same topology and they oscillate from one well to the other at the same frequency. In this case, if we start with a initial preparation at the north pole of our Bloch sphere (i.e. all bosons on the first site), we will observe Bloch oscillations, defined by the change of only \dot{S}_z , between the two wells. The frequency which defines the oscillations of the system for this case is $\omega_{osc} = k$.

As we increase u , but keep it less than 1, we find that the trajectories continue to share the same topology, but the frequency at which they oscillate begins to depend on the population imbalance. The value $u = 1$ is the critical point when a separatrix emerges in the phase space, dividing it into three parts: two islands and a sea. If the trajectory starts on an island, it is stuck doing small oscillations around the initial population imbalance, while if it starts in the sea, it will undergo Bloch-Josephson oscillations (in which both the population imbalance and φ change).

Since we are working with a system whose initial preparation corresponds to all particles being on the north pole, another critical value of u is $u \sim 2$. Before we reach this point, the separatrix does not touch the north pole, thus not affecting the behavior of the system. At $u \sim 2$, the separatrix just reaches the north pole (as well as the south, in the symmetric potential), dominating the dynamics of the system.

Once $u \gg 2$, the islands created by the separatrix encircle the north and south pole, inducing self-trapping behavior for our initial state. If in this limit, we start with a preparation of trajectories along or near the equator (e.g. a quantum state $|N/2, N/2\rangle$), we would observe Josephson oscillations (i.e. changing φ) with a frequency $\omega_{osc} = \sqrt{NUk}$. When we start at the north pole in the limit of $u \gg 2$, then we will see self-trapped behavior with small oscillations of $\omega_{osc} = NU$ (see Appendix B). To summarize

3 Dynamics of the Symmetric Dimer

(see Fig. 3.5):

$$\omega_{osc} = \begin{cases} k & \text{for } u \ll 1 \\ NU & \text{for } u \gg 1, \text{ initial condition on the poles} \\ \sqrt{NUk} & \text{for } u \gg 1, \text{ initial condition on the equator} \end{cases} \quad (3.23)$$

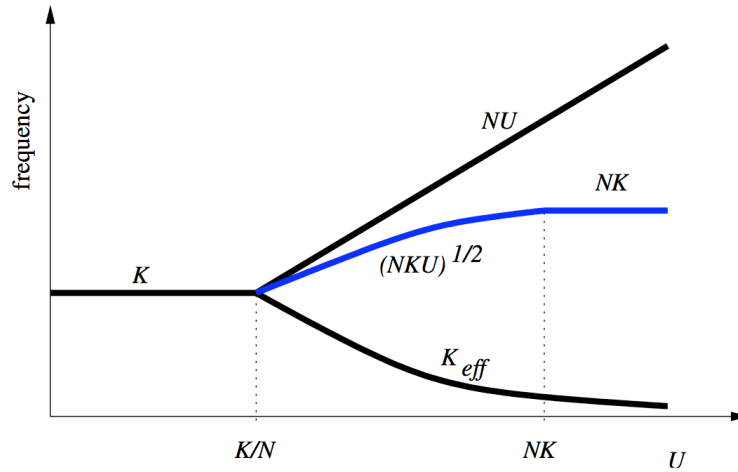


Figure 3.5: The various frequencies involved in determining the wavepacket dynamics as they depend on U . For the sake of completeness, we have also included the quantum frequency k_{eff} .

The work done by the Oberthaler group in Heidelberg shows that for large numbers of bosons and short times, classical analysis works well to describe the evolution of the population imbalance [1], as shown in Fig. 3.6. However, when we decrease the number of bosons in our system, quantum effects become more prevalent, and the classical expectations no longer match the quantum results (see Fig. 3.3). Since the quantum-classical correspondence breaks down fairly quickly when we have few particles in our system, we need to employ a different technique to model the behavior, which we do in §3.5.

3 Dynamics of the Symmetric Dimer

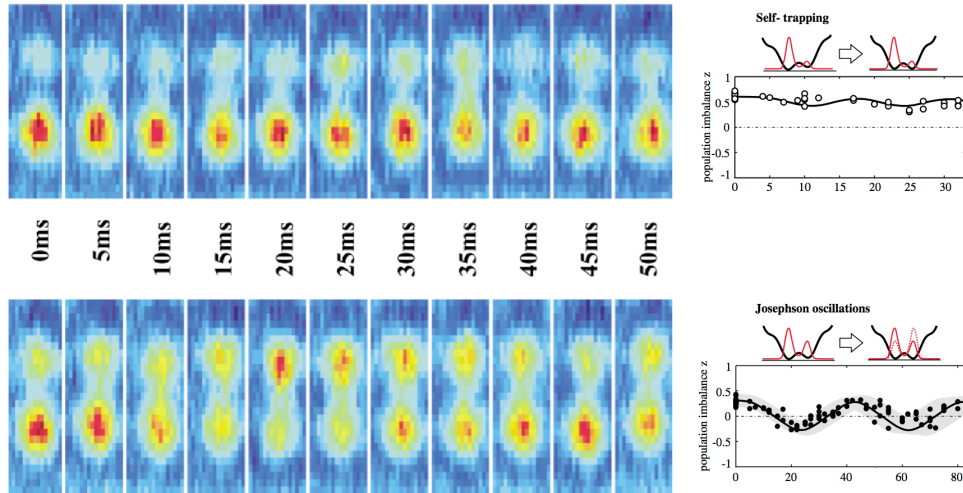


Figure 3.6: On the left we show the results of Oberthaler’s group - the top section corresponds to the self-trapping regime, while the bottom corresponds to the Josephson oscillation regime. On the right the experimental results for the population imbalance for both regimes are plotted as dots, while the classical predictions from Eqs. 3.14 and 3.15 are shown as black lines. In this time scale with $N \sim 1000$ particles, the classical equations of motion match the experimental results. Figures taken from [1].

An alternative representation: The DNLS

In §2.4, we introduced the mean-field approach as a possible way to describe the dynamics of a Bose-Einstein condensate trapped in a lattice. The equation in its discrete form is known as the Discrete Nonlinear Schrödinger equation [Eq. (2.20)]

$$i\dot{A}_j = \varepsilon_j A_j + UN |A_j|^2 A_j - \frac{k}{2} (A_{j-1} + A_{j+1}) \quad (3.24)$$

where $A_j = \sqrt{n_j} e^{i\varphi}$. The derivation of the DNLS assumes that our wavepacket evolves coherently - in other words, if we begin with a binomial distribution ($P_n(t) = p^n (1 - p)^{N-n}$, where p is the probability to be in site 1), we will end up in a binomial distribution at the end of our evolution. As the packet is assumed to be binomial, the dynamics is characterized by $\langle n \rangle = pn$. In the case that $u = 0$, this is in fact true, and the mean-field description can be used to model the system. However, once the nonlinear interaction

3 Dynamics of the Symmetric Dimer

begins to affect the dynamics, the mean-field approach only holds up until the Ehrenfest time ($\sim \ln[N]$). The Ehrenfest time is not particularly long and as we increase u , the mean-field description becomes less accurate. For example, in Fig. 3.10, the $P_n(t)$ for $u = 2$ can clearly not be captured with the mean-field binomial distribution. Therefore, as stated earlier, we move to a different analytical technique, known as semiclassical analysis.

3.5 Semiclassical Analysis

As we discussed previously, the corresponding classical phase space is given by the Bloch sphere \mathcal{S}^2 . In this representation, the z -component of the Bloch vector describes the population imbalance between the two wells. The state $|N, 0\rangle$ is located at the north pole of the Bloch sphere, while the state $|0, N\rangle$ is at the south pole. For a quantum state with a well-defined angular momentum in the z -direction (i.e. an eigenstate of J_z), the other two angular momentum components J_x and J_y are unknown, since they do not commute with J_z . Thus, the azimuthal angle φ , also cannot be determined. Since, for a fixed number of particles N , the dimensionality of the Hilbert space is $N + 1$, the total phase space area is:

$$\text{span}(J_z) \times \text{span}(\varphi) = (N + 1) \times 2\pi. \quad (3.25)$$

Using the notation $S_x \equiv J_x/(N/2) = \sin(\theta) \cos(\varphi)$, $S_y \equiv J_y/(N/2) = \sin(\theta) \sin(\varphi)$ and $S_z \equiv J_z/(N/2) = \cos(\theta)$, we can rewrite the above relation as

$$\text{span}(S_z) \times \text{span}(\varphi) = 2 \times 2\pi \quad (3.26)$$

which is the surface area of the sphere of unit radius. For large numbers of particles, the difference between N and $N + 1$ becomes negligible and thus the effective Planck's constant, \hbar_{eff} , the area per state, is $\hbar_{eff} = 4\pi/N$.

Using the $\theta - \varphi$ uncertainty relation we can conclude that any S_z (or J_z state) is

3 Dynamics of the Symmetric Dimer

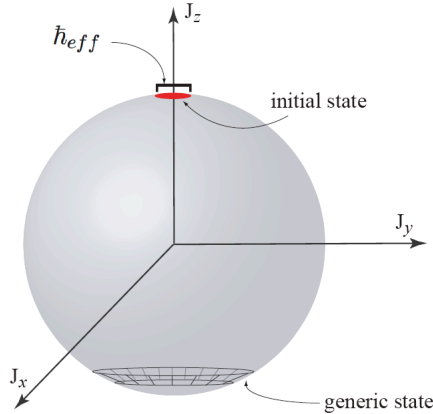


Figure 3.7: Representation of generic $|n, N - n\rangle$ state and the initial state, $|N, 0\rangle$, of the S_z operator in the Bloch sphere.

represented on the Bloch sphere by an annulus of width $\delta\theta = 2/(N+1)$ and circumference 2π . The case of an initial state $S_z = 1$ (where all particles are on the "left" well), is represented by a cap of area $4\pi/(N+1)$ (i.e. \hbar_{eff}) centered at the "north pole." An illustration of the state vectors on the Bloch sphere can be seen in Fig. 3.7.

We now turn to the Hamiltonian Eq. (3.11) which describes our dimer model. Within the semiclassical approximation, a quantum state is described as a distribution in phase space and the eigenstates are associated with stripes (i.e. lines of non-zero width) that are stretched along the contour lines $H(\varphi, \theta) = E$. The energy levels E_n of the dimer can be determined via WKB quantization of the phase space area enclosed by the contours. In the symmetric dimer, the contours of constant energy on the Bloch sphere (see Fig. 3.4) correspond to the eigenenergies of our system.

A classical phase space distribution $P^{cl}(S_z, \varphi; t)dS_z d\varphi$ describes the probability that an ensemble of particles will be found in an infinitely small phase space element, $dS_z d\varphi$. The dynamics of the Hamiltonian H is governed by the classical Liouville equation

$$\frac{dP_n^{cl}(s_z, \varphi; t)}{dt} = \frac{\partial P_n^{cl}(s_z, \varphi; t)}{\partial t} + \left\{ P_n^{cl}(s_z, \varphi; t), H_{PB} \right\} = 0 \quad (3.27)$$

where $\{\dots\}$ denote the classical Poisson brackets. One can evaluate the Liouvillian flow directly by making use of a classical phase space ensemble as shown in Fig. 3.9. To do the semiclassical calculations, we distribute an ensemble generated by 10^4 phase space

3 Dynamics of the Symmetric Dimer

points meant to mimic the quantum distribution throughout the $4\pi/N$ north pole cap. Then we allow all the trajectories to evolve according to the classical equations, Eqs. 3.14 and 3.15.

Using the outcome of the semiclassical approach we have evaluated the population imbalance in Fig. 3.8. The matching between the semiclassical and quantum results contrasts sharply with the classical calculations shown in Fig. 3.3. Clearly, we see that the semiclassical approach captures various features of the quantum evolution. In fact, the agreement seems to persist for relatively large times and u , as opposed to the "one-trajectory" classical calculation, which breaks down after a relatively short time.

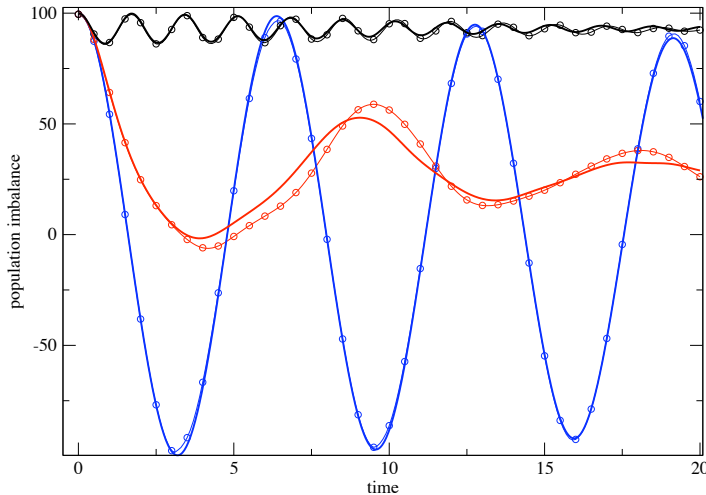


Figure 3.8: The temporal evolution of atomic population imbalance for $N = 100$ with the same values of u as Fig. 3.3. The quantum numerical results are shown as thick solid lines, while the semiclassical calculations are lines with circles. The initial ensemble consists of 10^4 trajectories and populates the north pole cap (as discussed in the text). Compare this to the classical results shown in Fig. 3.3.

Inspired by the excellent agreement shown between the semiclassical calculations and the exact quantum results in the first moment (described by the population imbalance), shown Fig. 3.8, we would like to investigate the applicability of semiclassical methods to

3 Dynamics of the Symmetric Dimer

describe the full occupation distribution, $P_n(t)$. In Fig. 3.9, we compare the semiclassical distribution $P_n^{\text{cl}}(t)$ with the exact quantum mechanical results $P_n(t)$ where we observe a reasonably good agreement.

Looking more closely at the wavepacket dynamics for a specific time, we see that the separatrix in the phase space crosses the north pole of the Bloch sphere. Therefore the wavepacket stretches along it as illustrated in Fig. 3.10 (the quantum results are shown in the top row, while the semiclassical calculations are shown in the second row). Note that this type of dynamics cannot be properly modeled by the mean-field approximation. The mean-field equation merely describes the Hamiltonian evolution of a single point in phase space and therefore assumes the wavepacket looks like a binomial distribution at any moment. Whenever the motion is in the vicinity of the separatrix, the mean-field approach becomes inapplicable and thus $P_n(t)$ is not likely to be binomial (see bottom row of Fig. 3.10).

3 Dynamics of the Symmetric Dimer

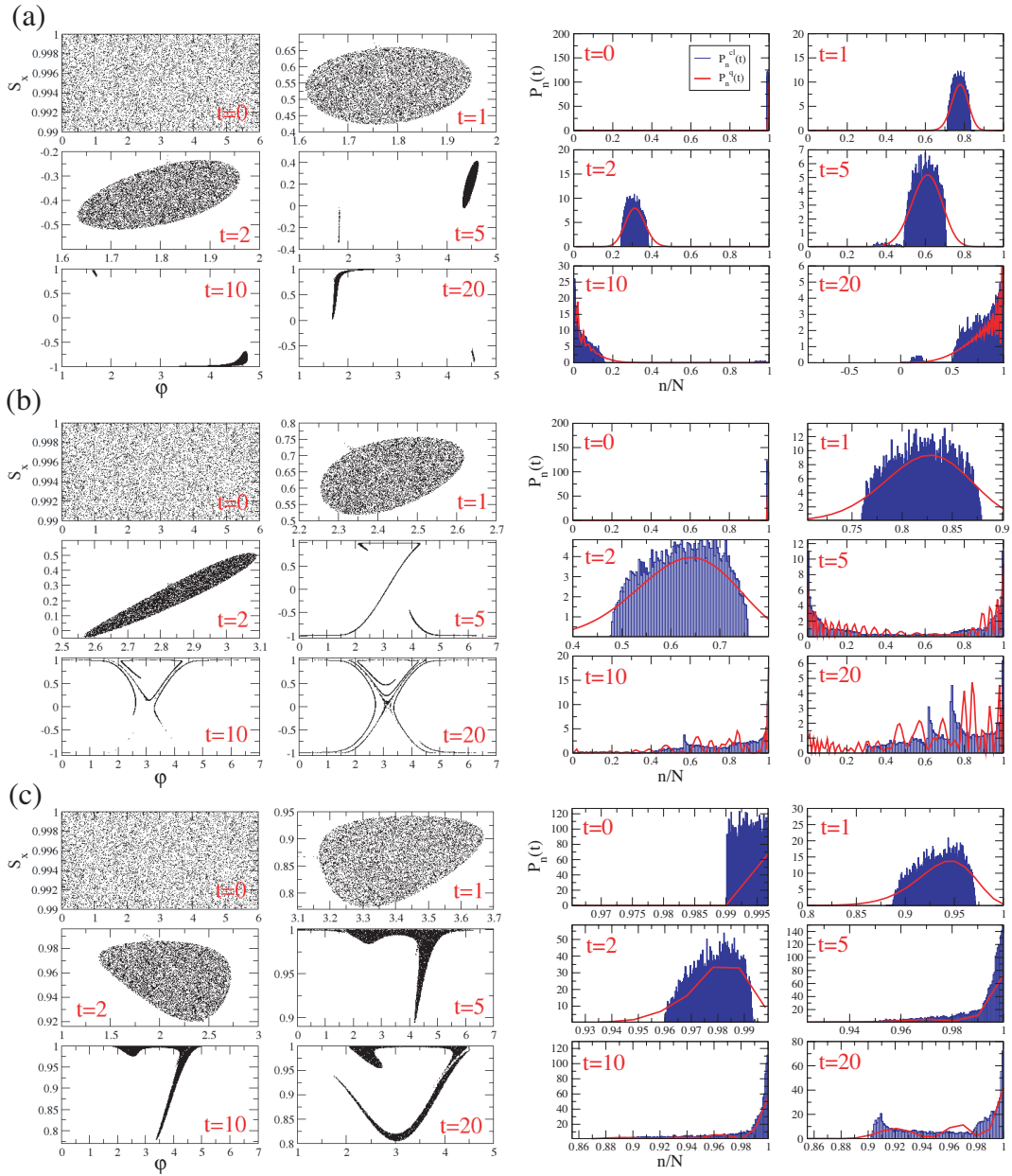


Figure 3.9: In the left column are snapshots of the evolving phase space distribution of an initial preparation associated with the quantum state $|N, 0\rangle$, where $N = 100$. The semiclassical distribution consist of 10^4 trajectories which are prepared as discussed in the text. In the right column, the semiclassical and the quantum evolving occupation probability are shown. The classical results are shown as blue histograms, while the quantum results are shown as red lines. A good quantum-classical correspondence is evident even for relatively large times. The rows correspond to different values of \tilde{U} : (a) $u = 0.5$, corresponding to the JJ regime. (b) Transition point $u = 2$. (c) Self-trapping regime, $u = 4$.

3 Dynamics of the Symmetric Dimer

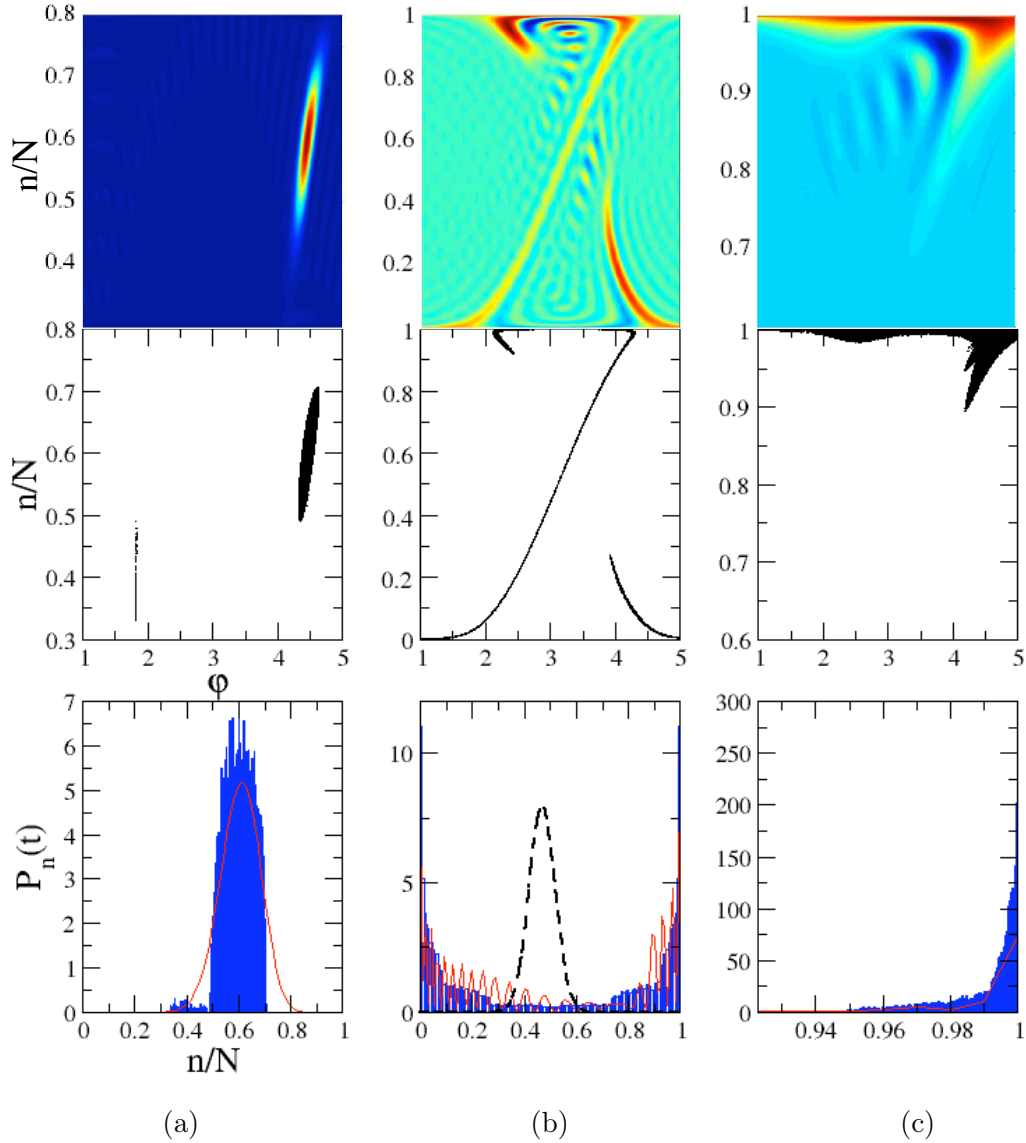


Figure 3.10: Dynamical evolution at $t = 5$ of a system of $N = 100$ for various values of u . The columns are for (a) $u = 0.5$, (b) $u = 2$, (c) $u = 4$. The top row is the Wigner representation of the quantum state. The second row is the classical phase space distribution obtained from the semiclassical calculations. The third row are the occupation statistics for the semiclassical (blue) and quantum (red) calculations. The semiclassical $P_n(t)$ is found by taking a histogram of the classical phase space distribution in the second row. To contrast the mean-field $P_n(t)$ with the semiclassical and quantum for motion near the separatrix, the binomial distribution is plotted as a black dashed line in (b).

4 Landau-Zener Transitions

Generic systems are described by a Hamiltonian $H(P, Q; x)$, which depends not only on position and momentum coordinates, Q and P , but also on some parameter x . In many systems of physical interest, x is a time-dependent parameter, i.e. $x = x(t)$. In these cases, the energy of the system is no longer a constant of motion and the system "transitions" between energy levels. Such a system can be modeled using a so-called 'system-bath' model dividing the system into a subsystem (which we want to study) and the environment (a reservoir) [54]. As $x(t)$ changes, the environment absorbs energy. This irreversible change of energy is known as dissipation. The rate of driving (i.e. the change of the time-dependent parameter) $\dot{x}(t)$ and the strength of the perturbation allow one to distinguish various regimes of quantum dissipation (see §5.1).

This chapter is principally concerned with the limit of a small $\dot{x}(t)$. In this case, the energy is dissipated via Landau-Zener transitions between the levels $E_n(x)$ experiencing avoided crossings as the driving parameter $x(t)$ is changed (see, for example, Fig. 4.1). When the gap ΔE in an avoided crossing is sufficiently small, there is a finite probability of a particle making a non-adiabatic transition from one energy level to another, i.e. from the occupied state to an unoccupied state. Clarence Zener studied this process for an avoided crossing in a two-level system [59].

We begin this chapter by presenting some physical examples of parametric Hamiltonians. We will then address the Landau-Zener transition probability, including the adiabatic approximation and the equations of motion for a time-varied system. Finally, we will work through a two level system (a spin 1/2 particle in a driven magnetic field)

4 Landau-Zener Transitions

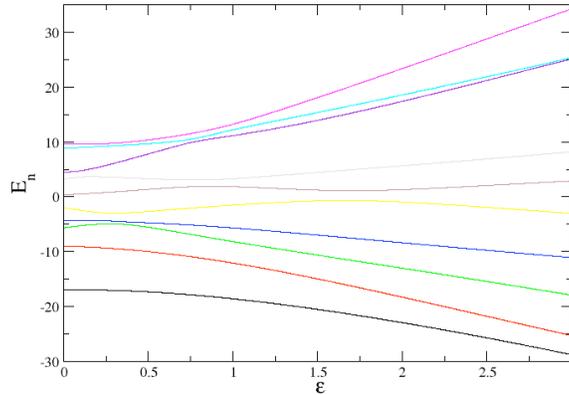


Figure 4.1: This is the parametric level evolution of the Hamiltonian H versus the perturbation ε . The Hamiltonian is $H = H_0 + \varepsilon B$, where H_0 and B are both banded random matrices with a Gaussian distribution and a bandwidth of b . In this graph, the level evolution is done for $b = 5$ and system size of 10. Courtesy of Mei Chai Zheng.

and find the Landau-Zener transition probability of this simple system.

4.1 Parametric Hamiltonians and their Applications

It is the rule, rather than the exception that physical setups are described by parametric Hamiltonians $\mathcal{H}(Q, P; x(t))$ [55]. One example of such a system is the 'piston model' in which a particle is trapped inside an enclosure with a moving wall. The location of this wall, or piston, is described by the coordinate $x(t)$. This system is illustrated in Fig. 4.2a. If the piston is much more massive than the particle, then $x(t)$ represents the coordinate of a degree of freedom that is weakly perturbed by the rest of the system - i.e. the motion of the particle in the cavity, affected by the piston, only mildly affects $x(t)$, the position of the piston. The piston model itself is a prototype for many systems which can be described by parametric Hamiltonians.

The nuclei of a molecule are akin to the piston model. In this system, $x(t)$ represents the motion of the nuclei, thus producing a Hamiltonian which describes the changes in

4 Landau-Zener Transitions

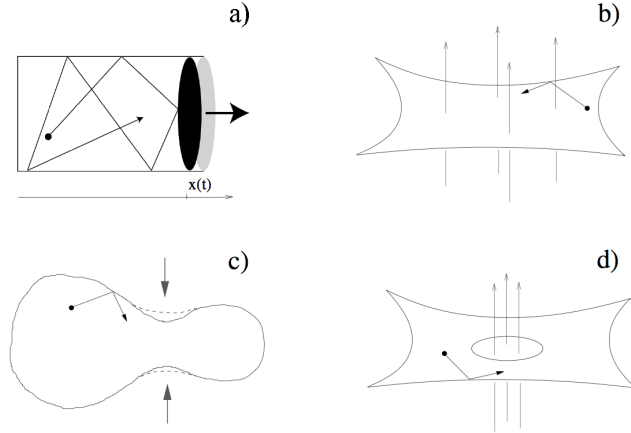


Figure 4.2: Various applications of parameter-dependent Hamiltonians. (a) The piston model where $x(t)$ represents the position of the piston. (b) A small magnetic particle influenced by a magnetic or electric field of strength $x(t)$. (c) The 'Liquid Drop Model' of the nucleus, where $x(t)$ is parameterizes the shape of the drop. (d) A magnetic flux, $x(t)$, passing through a conduction loop. Figure taken in part from Ref. [23].

the electronic degrees of freedom for a fixed configuration of the nuclei. Just as in the piston model, the mass of the nuclei is huge in comparison to that of the electrons, thus electrons only weakly affect the coordinate $x(t)$.

Another application of the parametric Hamiltonian is to a small metal particle being perturbed by an electric or magnetic field, which is represented by $x(t)$. Within the metal particle, the electrons align in phase or out of phase with the field, thus weakly perturbing $x(t)$. This system is illustrated in Fig. 4.2b.

The 'liquid drop model' of the nucleus also uses a parametric Hamiltonian. In this model, the nucleus is represented by a drop of nuclear liquid inside which the nucleons move. The nucleons are imagined to interact so strongly that their mean free path is much less than the nuclear radius, thus allowing them to move almost independently with respect to the walls of the 'liquid drop.' In this system, $x(t)$ could correspond to the parameterization of the shape of the droplet, as shown in Fig. 4.2c.

The final example we will present originates in mesoscopic physics. The system is made up of a conducting ring threaded by a magnetic flux. Here $x(t)$ represents the

4 Landau-Zener Transitions

magnetic flux through the hole in the ring [8]. The rate at which the flux changes determines the electromotive force induced by Faraday's Law ($emf = -\dot{x}(t)$). The emf establishes a current around the ring which is proportional to the emf itself. The proportionality factor is the conductance G . This is, in fact, Ohm's law. The dissipation energy in this system can either be accumulated by the electrons as kinetic energy or it may be transferred to the lattice vibrations. The latter case heats up the ring. The rate at which the ring heats up is found, via Joule's law, to be proportional to the square of the emf .

4.2 Adiabatic Approximation and Equations of Motion

The simplest way to understand the parametric Hamiltonian is to split it into time-dependent and time-independent parts:

$$H(t) = H_0 + H_t \quad (4.1)$$

At each moment in time, the state vector of the system can be written in the instantaneous (or adiabatic) basis

$$|\psi(t)\rangle = \sum_n a_n(t) |\varphi_n(t)\rangle \quad (4.2)$$

Via Schrödinger's Equation $i\hbar \frac{d}{dt} |\psi(t)\rangle = H(t) |\psi(t)\rangle$, we find

$$i\hbar \left[\sum_n \dot{a}_n(t) |\varphi_n(t)\rangle + \sum_n a_n(t) \frac{d}{dt} |\varphi_n(t)\rangle \right] = \sum_n a_n(t) E_n(t) |\varphi_n(t)\rangle. \quad (4.3)$$

When we multiply from the left with $\langle \varphi_m(t) |$ the sums collapse:

$$i\hbar \dot{a}_m(t) = a_m(t) E_m(t) - i\hbar \sum_n a_n(t) \langle \varphi_m(t) | \frac{d}{dt} |\varphi_n(t)\rangle \quad (4.4)$$

In order to solve Eq. (4.4) we need to understand how to evaluate $\langle \varphi_m(t) | \frac{d}{dt} |\varphi_n(t)\rangle$.

4 Landau-Zener Transitions

Thus, we look at the time derivative of the Schrödinger Equation multiplied by $\langle \varphi_m(t) |$

$$\langle \varphi_m(t) | \frac{d}{dt} [H(t) | \varphi_n(t) \rangle] = \langle \varphi_m(t) | \frac{d}{dt} [E_n(t) | \varphi_n(t) \rangle] \quad (4.5)$$

which allows us to find an expression for the problem term

$$\langle \varphi_m(t) | \frac{d}{dt} | \varphi_n(t) \rangle = \frac{\dot{V} \langle \varphi_m(t) | \frac{dH(t)}{dV} | \varphi_n(t) \rangle - \dot{E}_n \delta_{mn}}{E_n - E_m}. \quad (4.6)$$

We can then plug this into Eq. (4.4), constraining the sum to $n \neq m$

$$\dot{a}_m(t) = -\frac{i}{\hbar} (E_m(t) - A_m) a_m(t) + i\hbar \dot{V}(t) \sum_{n \neq m} \frac{F_{mn}}{E_n - E_m} a_n(t) \quad (4.7)$$

where $F_{mn} = -\langle \varphi_m(t) | \frac{d}{dt} | \varphi_n(t) \rangle$ and $A_m = i\hbar \langle \varphi_m(t) | \frac{d}{dt} | \varphi_m(t) \rangle$.

As an initial step towards solving Eq. (4.7), we introduce a new constant $C_m(t)$ such that

$$a_m(t) = C_m(t) e^{-\frac{i}{\hbar} \int E_m(t') dt'}. \quad (4.8)$$

Note that the probability $|a_m(t)|^2$ remains unchanged in this transformation, i.e.

$$|a_m(t)|^2 = |C_m(t)|^2. \quad (4.9)$$

Substituting Eq. (4.8) into Eq. (4.7) and canceling like terms, we find

$$\dot{C}_m(t) = \frac{i}{\hbar} A_m(t) C_m(t) + \dot{V}(t) \sum_{n \neq m} \frac{F_{mn}}{E_n - E_m} C_n(t) e^{-\frac{i}{\hbar} \int [E_n(t') - E_m(t')] dt'}. \quad (4.10)$$

4.2.1 Adiabatic Condition

We recollect from the last section that $|\psi(t)\rangle = \sum_n a_n(t) |\varphi_n(t)\rangle$, where $\langle \varphi_m(t) | \varphi_n(t) \rangle = 0$. So, for adiabaticity, $a_n(t)$ cannot depend on $a_m(t)$. Therefore, the energy step made

4 Landau-Zener Transitions

due to the rate must be much less than the difference between the energy levels, i.e.

$$\dot{V}(t) \max \left| \frac{F_{mn}}{E_m - E_n} \right| \ll \min |E_m - E_n|. \quad (4.11)$$

We can define the minimum difference in energy as $\Delta = \min |E_m - E_n|$. Since the smallest gap between energy levels is of the order of k we can state

$$\dot{V} \ll \frac{\Delta^2}{|F_{mn}^{(max)}|} \sim k^2 \quad (4.12)$$

which is the adiabatic condition.

When the adiabatic condition holds, Eq. (4.7) becomes

$$\frac{da_m}{dt} = -\frac{i}{\hbar} (E_m(t) - A_m) a_m(t) \quad (4.13)$$

enabling us to solve for $a_m(t)$

$$a_m(t) = a_m(0) e^{-\frac{i}{\hbar} \int_0^t E_m(t') dt'} e^{\int_0^t \dot{V}(t') \langle \varphi_m(t') | \frac{d}{dV} | \varphi_m(t') \rangle dt'}. \quad (4.14)$$

This can be simplified to

$$a_m(t) = a_m(0) e^{-\frac{i}{\hbar} \int_0^t E_m(t') dt'} e^{\int_{V_0}^{V_f} \langle \varphi_m | \frac{d}{dV} | \varphi_m \rangle dV}. \quad (4.15)$$

4.2.2 Geometric Phase

In Eq. (4.15), two phases are evident. The first,

$$-\frac{i}{\hbar} \int_0^t E_m(t') dt' \quad (4.16)$$

4 Landau-Zener Transitions

is the dynamical phase, which generalizes the standard time evolution factor to account for energies levels which are dependent on time. The second

$$\gamma_m(t) = \int_{V_0}^{V_f} \langle \varphi_m | \frac{d}{dV} | \varphi_m \rangle dV \quad (4.17)$$

is the geometric, or Berry's, phase.

When the Hamiltonian is evolved such that after some time T it returns to its original state, then Berry's phase becomes:

$$\gamma_m(T) = \int_{V_0}^{V_0} \langle \varphi_m | \frac{d}{dV} | \varphi_m \rangle dV. \quad (4.18)$$

If only one parameter in the Hamiltonian changes, then Eq. (4.18) easily simplifies to $\gamma_m(T) = 0$. However, if multiple parameters are changing, then $\gamma_m(t)$ is not so straightforward. In this case, Berry's phase is

$$\gamma_m(t) = \int_{\vec{V}_0}^{\vec{V}_f} \langle \varphi_m | \nabla_V | \varphi_m \rangle \cdot d\vec{V}, \quad (4.19)$$

which, when $\vec{V}_0 = \vec{V}_f$ becomes

$$\gamma_m(T) = \oint \langle \varphi_m | \nabla_V | \varphi_m \rangle \cdot d\vec{V}. \quad (4.20)$$

This line integral is generally not zero. Note that while Berry's phase is dependent on how the multiple parameters of the Hamiltonian change, it is not dependent on how fast they do so.

4 Landau-Zener Transitions

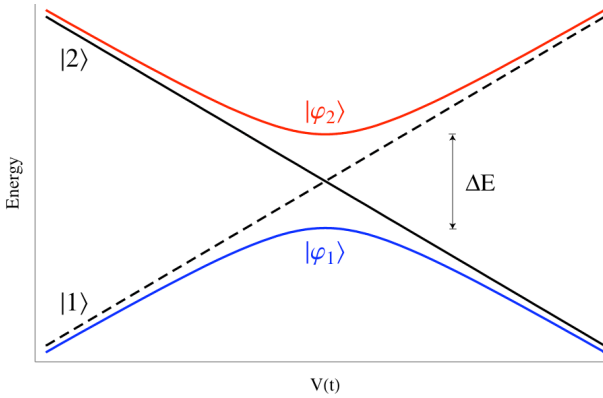


Figure 4.3: Avoided energy level crossings. The diabatic states are represented by $|1\rangle$ and $|2\rangle$, while $|\varphi_1\rangle$ and $|\varphi_2\rangle$ represent the adiabatic states.

4.3 Example: A spin in a magnetic field

A spin in an external magnetic field is an illustrative example of avoided crossing behavior. The Hamiltonian for this system, written in the diabatic basis, is

$$H = \frac{1}{2}(V(t)\sigma_z + k\sigma_x) = \frac{1}{2} \begin{bmatrix} \alpha t & k \\ k & -\alpha t \end{bmatrix} \quad (4.21)$$

where $V(t) = \alpha t$ and k is the coupling between the two diabatic states of the system. The energies for this system are

$$E_{\pm}(t) = \pm \frac{1}{2}\Omega \quad (4.22)$$

where $\Omega = \sqrt{(\alpha t)^2 + k^2}$. The eigenvectors for the spin in a magnetic field become the diabatic states and can be given by

$$|+\rangle = \frac{1}{\sqrt{2}} \begin{bmatrix} \sqrt{1 + \sin\theta} \\ \sqrt{1 - \sin\theta} \end{bmatrix}; \quad |-\rangle = \frac{1}{\sqrt{2}} \begin{bmatrix} \sqrt{1 - \sin\theta} \\ -\sqrt{1 + \sin\theta} \end{bmatrix} \quad (4.23)$$

where $\tan\theta = \alpha t/k = \tau$.

We want to investigate the probability of moving from $|\varphi_1\rangle$ to $|\varphi_2\rangle$. In order to do so, we need to calculate the quantities A_m and F_{mn} of Eq. (4.10). The former necessitates

4 Landau-Zener Transitions

a time derivative of $|+\rangle$ and $|-\rangle$:

$$\frac{d}{dt}|+\rangle = \frac{\dot{\theta}}{2}|-\rangle; \quad \frac{d}{dt}|-\rangle = -\frac{\dot{\theta}}{2}|+\rangle \quad (4.24)$$

Thus, clearly $A_{\pm} = 0$ in this system. To find F_{mn} we use $\frac{dH}{dV} = \sigma_z/2$:

$$F_{mn} = -\frac{k}{2\Omega}. \quad (4.25)$$

Eq. (4.10) thus becomes

$$\dot{C}_+ = \frac{1}{2} \frac{1}{1 + \tau^2} C_-(t) e^{\frac{i}{\hbar} \int \Omega(t') dt'}. \quad (4.26)$$

The integral in the dynamical phase, $\int \Omega(t') dt'$, can be rewritten as

$$\int \Omega(t') dt' = \int k \sqrt{\frac{(\alpha t')^2}{k} + 1} dt' = \frac{k^2}{\alpha} \int \sqrt{\tau'^2 + 1} d\tau'. \quad (4.27)$$

Therefore, the probability to transition to the $|+\rangle$ state from the $|-\rangle$ state is

$$P_{LZ} = |a_+|^2 = |C_+|^2 = \left| \frac{1}{2} \int_{-\infty}^{+\infty} \frac{1}{1 + \tau^2} C_-(\tau) e^{\frac{i}{\hbar} \frac{k^2}{\alpha} \int \sqrt{\tau'^2 + 1} d\tau'} d\tau \right|^2. \quad (4.28)$$

Beginning completely in the $|-\rangle$ state, we approximate $C_- \approx 1$. Doing an integration over the complex plane, we find

$$P_{LZ} \approx \left(\frac{\pi}{3}\right)^2 \exp\left(-\frac{\pi k^2}{4 \alpha}\right). \quad (4.29)$$

5 Dynamics of the Driven Dimer

The study of wavepacket dynamics is a simple, yet vital, step towards understanding the dynamics of a BEC loaded in a double well potential. In this chapter we move to the more demanding situation of a driven dimer. In studying this system, we will assume that the potential difference between the two wells is changing at a constant rate and analyze the evolution of the occupations statistics (i.e. the evolving probability occupation) utilizing the concepts introduced in the previous chapter. Depending on the interatomic interaction and the rate at which we change the onsite potential difference, we find three different dynamical scenarios: adiabatic, diabatic, and sudden. The structure of this chapter is as follows: The first section of this chapter will introduce our motivations for studying a BEC trapped in a driven dimer. Then we will go on to define two genres of regimes, each containing three different dynamical scenarios. Finally, we will discuss our theoretical and numerical results for the asymptotic occupation distribution in these regimes, including a scaling relation we created to demonstrate the link between average atomic population and its variance.

5.1 Motivations for Study

The overarching motivation for research on an atomic BEC in a driven double well potential is the study of quantum dissipation in the presence of many-body interactions. When a system is driven, the energy is no longer a constant of motion. Instead, the system makes transitions between energy levels and thus the energy distribution evolves with time. Loosely speaking, the problem of quantum dissipation is to find a theory

for this evolution. At this point, the classical theory of dissipation is well understood. However, the quantum theory of dissipation still has many exciting open questions. One of the major areas of study is quantum dissipation of chaotic systems. An extension of a global theory for the dynamics of undriven chaotic systems is expected to further the formation of a universal (i.e. system independent) theory for quantum dissipation [12, 55]. Recent studies have concluded that in quantum dissipation of chaotic systems one can distinguish between four different dissipation mechanisms. These mechanisms depend on the strength of the perturbation and the frequency of the driving. The first of these is the adiabatic Landau-Zener regime, which corresponds to the very slow driving of the system we discussed in Chapter 4. The second regime is the perturbative regime, in which the driving is still small, but can be accurately described using first order time-dependent perturbation theory. As the driving is increased further, the underlying mechanism of dissipation is dictated by Fermi's Golden Rule transitions between the energy levels. This use of Fermi's Golden Rule incorporates infinite order perturbation theory, thus it breaks down when the system moves to the non-perturbative (fourth) regime (where there are quantum mechanically strong perturbations) [12]. Another intense area of study in quantum dissipation are the effects of many-body interactions on the transition probability between energy levels. One of the questions asked in this context is how the traditional (one-particle) Landau-Zener mechanism discussed in Chapter 4 is affected by these many-body interactions.

The driven double well potential provides a simple model to study these questions both experimentally and theoretically. In addition, due to the mathematical and experimental simplicity of the system, its study can allow us to understand the relation between microscopic theories governed by quantum mechanics and macroscopic theories governed by classical considerations. One fundamental question in the framework of quantum dissipation is the determination of the semiclassical limit, which goes hand-in-hand with quantum-classical correspondence (QCC) considerations.

In this respect, one can distinguish between two regimes of QCC: (i) detailed QCC,

5 Dynamics of the Driven Dimer

in which all of the moments of the observable occupation distribution correspond to classical results, and (ii) restricted QCC, in which only some moments of the quantum and classical occupation distributions match [49]. We are interested in studying the full counting statistics (FCS) of the dimer (or equivalently, in our case, the full occupation statistics, as shown in Appendix C).

Studying the FCS of an atomic BEC in a driven dimer is also beneficial to the field of mesoscopic electronics. In electronic devices a type of noise called “shot noise” can occur when the number of electrons is small enough to create detectable statistical noise in the measurement. Shot noise is important to study in electronics due to the advent of low-power circuits in an era of energy-consciousness [41]. To understand shot noise, it is necessary to study both the average occupation number and its variance [6]. In the study of atom currents it is desirable to control the flow to one atom at a time. As one can infer, it is important to understand all possible sources of noise that corrupt the atomic current, as this will allow us to optimize information transfer. The dimer allows us to study the flow of atoms from one location to another, and therefore, to better understand how noise can be controlled, we study the full counting statistics of the system, both classically and quantum mechanically [10].

Early work on the fundamental questions regarding QCC in the driven dimer led to a paradox in the commutability of the semiclassical with the adiabatic limit [25]. As we established in the last chapter, a parametric Hamiltonian has some time-dependence

$$i\hbar \frac{\partial}{\partial t} |\psi\rangle = H(f(\dot{e}t)) |\psi\rangle. \quad (5.1)$$

In 1977, Hwang and Pechukas [25] claimed that by rescaling time $\tau = \dot{e}t$ and defining an effective Planck’s constant $\hbar_{eff} = \dot{e}\hbar$, one could show that the semiclassical limit $\hbar \rightarrow 0$ and the adiabatic limit $\dot{e} \rightarrow 0$ were equivalent, since in both cases, $\hbar_{eff} \rightarrow 0$. Berry was the first to refute this argument. He showed that in a non-interacting system, such as the driven dimer populated by one boson, the Landau-Zener transition P_{LZ} is zero in the

adiabatic limit, while there is 100% probability to transition in the semiclassical limit [5]. Wu and Liu further expanded on Berry's work by addressing the driven double well potential for an $N > 1$ particle system with interatomic interactions [57]. They found when the tunneling rate k is less than the interaction strength UN , the semiclassical and adiabatic limits did not match up for slow rates. However, when $k > UN$, the P_{LZ} match for both the quantized and classical model when $\varepsilon \rightarrow 0$. The difference between these two regimes will be discussed in §5.4. The final step, which would close the chapter on this controversy would be an experimental test of the commutability between the semiclassical and adiabatic limits.

As a result of these motivations, work began on the driven dimer in the first two regimes of quantum dissipation - the adiabatic and perturbative regimes. In contrast to our work, up until the present, all of the literature uses the mean-field approach to analyze the system. This work is discussed in the next section.

5.2 Mean-field Dynamics and Nonlinear Landau-Zener

Tunneling

For small driving rates, the transport between levels is dominated by LZ transitions between energy levels engaging in avoided crossings. Thus, to understand quantum-classical correspondence in the presence of interactions, LZ tunneling needs to be extended and investigated in the frame of mean-field theories. Due to its simplicity, the dimer is a choice model for such an investigation [34, 56, 58]. The DNLS introduced in §2.4 can be written in matrix form as

$$H = \begin{bmatrix} \varepsilon + U|A_1|^2 & -\frac{k}{2} \\ -\frac{k}{2} & U|A_2|^2 \end{bmatrix}, \quad (5.2)$$

calling to mind the Hamiltonian used in the Chapter 4. To understand the dimer populated by $N > 1$ bosons, we need to understand how the interatomic interactions between

5 Dynamics of the Driven Dimer

the atoms affect the dynamics of the system. Thus, one can plot the energy levels for Eq. (5.2) with and without interatomic interactions, as shown in Fig. 5.1. When $U < k$, the nonlinear eigenvalue problem Eq. (5.2) has two eigenvalues. Conversely, it has four when $U > k$, creating a loop structure in the energy levels when $|\varepsilon| < \varepsilon_c$.¹ The parametric evolution of the classical levels is shown for both cases in Fig. 5.1. The loop structure in the $U > k$ case creates an interesting phenomenon - the breakdown of adiabatic evolution, even in the adiabatic limit. We can, for example, begin with a state in the upper branch of the adiabatic level in Fig. 5.1b. When we move it along the level by changing ε very slowly, the state will follow the lower energy past point X to the terminal point T . Once reaching this point, it can go no further unless it jumps to either the upper or lower energy level. Since both jumps are discontinuous, we expect that there will be nonzero probability to move to the lower level. The tunneling probability needs to be adjusted to take into account the nonlinear interatomic interactions below and above the critical ratio $U/k = 1$ [34]:

$$P_{NLZ} \sim \begin{cases} P_{LZ}, & U = 0 \\ \exp\left(-q \frac{\pi k^2}{2\dot{\varepsilon}}\right), & U < k \\ 1 - \frac{\pi k^2}{2\langle\dot{\varepsilon}\rangle} & U > k \end{cases} \quad (5.3)$$

where

$$\begin{aligned} q &= \frac{4}{\pi} \int_0^{\sqrt{(k/U)^{2/3}-1}} (1+x^2)^{1/4} \left(\frac{1}{(1+x^2)^{3/2}} - \frac{U}{k}\right)^{3/2} dx \\ \langle\dot{\varepsilon}\rangle &= \dot{\varepsilon} + 2U \left(\frac{k}{2}\right)^2 \sqrt{\frac{\pi}{\langle\dot{\varepsilon}\rangle}} \end{aligned} \quad (5.4)$$

Recently, the focus shifted to the next step of comparing quantum mechanical results with classical ones in the adiabatic limit [56]. However, these authors confined their analysis to the first moment of the occupation probability.

¹for definition of ε_c , see Eq. (3.19)

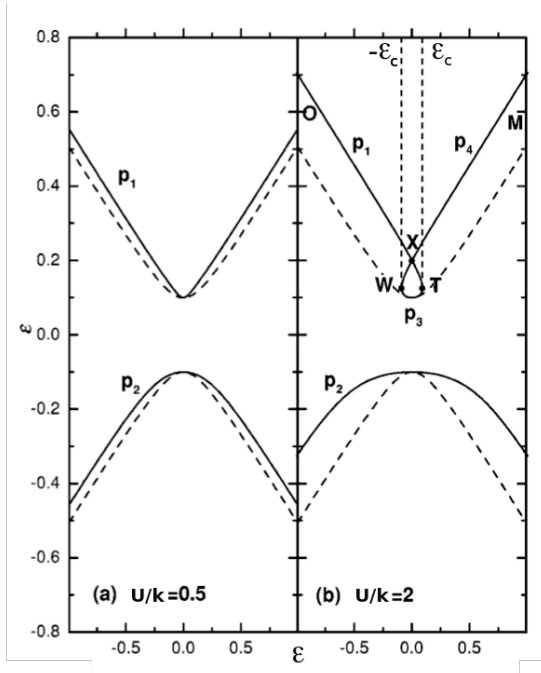


Figure 5.1: Adiabatic energy levels for the linear case (dashed lines) and nonlinear cases (solid lines). (a) shows the levels where $U/k < 1$ and (b) shows the levels where $U/k > 1$. Note the loop which appears in the lower energy level when the critical $U/k = 1$ is surpassed. Figure taken from [34].

5.3 The Bose-Hubbard Hamiltonian Formalism

Having researched the dynamics of the dimer while holding all parameters constant, we now wish to complicate our study by changing the onsite potential bias $\varepsilon = \varepsilon_2 - \varepsilon_1$ at some constant rate, such that $\varepsilon = \dot{\varepsilon}t$. As shown in Fig. 5.2, we begin with a very negative bias $\varepsilon = -a$ and allow the system to evolve to a very positive bias $\varepsilon = a$.² To study the many-body Landau-Zener transitions (LZ), we want to know how the driving rate $\dot{\varepsilon}$ affects the number of remaining atoms in the first well at the end of our evolution.

We continue to use the Bose-Hubbard Hamiltonian Eq. (2.21) to describe our system. Without loss of generality, we can assume that $\varepsilon_2 = 0$, thus only changing the onsite potential of the first well. With this in mind, we can rewrite the Hamiltonian as

$$\hat{H} = -\varepsilon\hat{n}_1 + \frac{U}{2} [2(\hat{n}_1^2 - N\hat{n}_1) + N^2 - 1] - \frac{k}{2} (\hat{b}_1^\dagger\hat{b}_2 + \hat{b}_2^\dagger\hat{b}_1) \quad (5.5)$$

²“Very” positive and negative means that $|a| \gg \varepsilon_c$, where again $\varepsilon_c = (u^{2/3} - 1)^{3/2}$.

5 Dynamics of the Driven Dimer

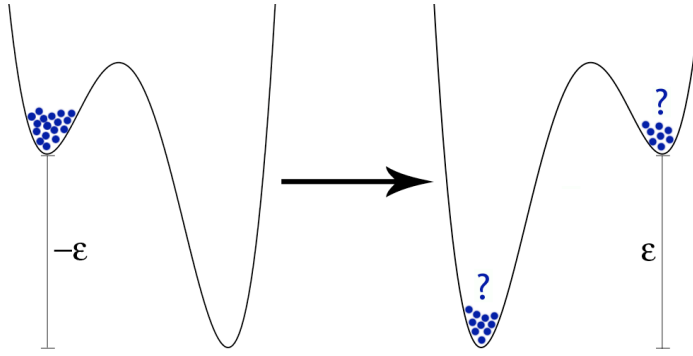


Figure 5.2: We drive our dimer by beginning with a very negative bias and ending our evolution with a very positive bias.

In addition to the BHH form of the Hamiltonian, we recall the SU(2) form

$$\hat{H} = U \hat{J}_z^2 + \varepsilon \hat{J}_z - k \hat{J}_x, \quad (5.6)$$

which becomes

$$H \approx \frac{Nk}{2} \left[\frac{u}{2} S_z^2 - \frac{\varepsilon}{k} S_z - \sqrt{1 - S_z^2} \cos \varphi \right] \quad (5.7)$$

in the semiclassical limit ($N \gg 1$). The equations of motion which are derived from the semiclassical limit are, as introduced in Chapter 3,

$$\dot{S}_z = -\sqrt{1 - S_z^2} \sin \varphi; \quad \dot{\varphi} = u S_z - \frac{\varepsilon}{k} + \frac{S_z}{\sqrt{1 - S_z^2}} \cos \varphi. \quad (5.8)$$

5.4 Dynamical Regimes

As indicated in Chapter 3, the interaction parameter $u = NU/k$ is crucial to the dynamics of the dimer, since it controls the classical phase space topology. In the driven double well potential, the driving rate $\dot{\varepsilon}$ also affects the occupation statistics. Therefore, we expect that the dynamics can be defined in a two-dimensional parameter space $(u, \dot{\varepsilon})$.

5.4.1 Interaction-dependent Regimes and the Parametric evolution of the energy levels

In order to understand the regimes defined by the interaction parameter u , we turn to the adiabatic evolution of the energy levels [24], in which we hold a chosen u constant while slowly stepping through values of the bias ε , as shown in Fig. 5.3. We will first assume that $u \gg 1$, then we will address the limit $u \ll 1$. In the former, the energies to zeroth-order approximation ($k = 0$) are

$$E_n = -\varepsilon n + \frac{U}{2} [2(n^2 - Nn) + N^2 - 1] \quad (5.9)$$

where n is the occupation of the left site. As shown in Chapter 2 (see Fig. 2.6), these energy levels vary linearly with the bias ε . However, the energy levels have different slopes, causing them to cross. We can estimate the crossing points ε_n by imposing the degeneracy condition $E_n = E_{n+1}$:

$$\varepsilon_n = U(2n - N - 1). \quad (5.10)$$

Consequently, the crossing spectrum ε_n occurs in the range

$$-U(N - 1) \leq \varepsilon \leq U(N - 1). \quad (5.11)$$

with an average distance between the crossings $\Delta\varepsilon = 2U$.

The width of the avoided crossings is determined by the coupling term in the Hamiltonian, Eq. (2.22), and is

$$\delta\varepsilon_n = \kappa_n; \quad \kappa_n = \frac{k}{2} \sqrt{n(N - n + 1)}. \quad (5.12)$$

The widest avoided crossing occurs at $n = N/2$, i.e. at the center of all of the crossings, with $\delta\varepsilon_n \sim Nk$. In order for all of the avoided crossings to be distinct, the width

5 Dynamics of the Driven Dimer

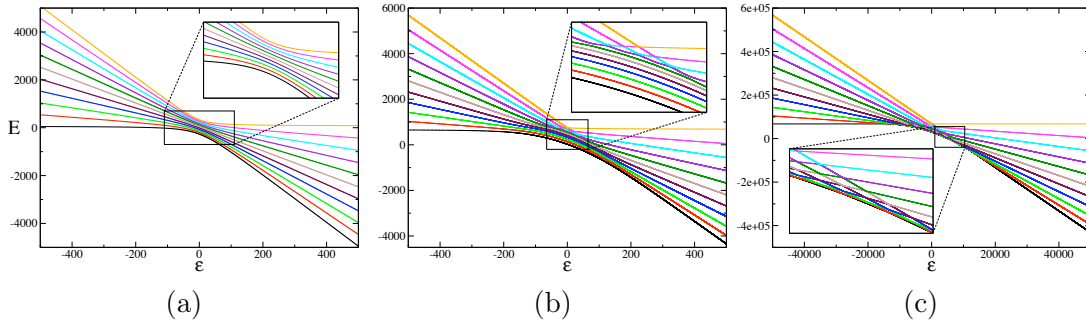


Figure 5.3: The parametric energy level evolution of 10 bosons loaded in the driven dimer for various u -regimes. (a) The mega crossing regime ($u = 0.25$), (b) The gradual crossing regime ($u = 2.5$), (c) The sequential crossing regime ($u = 250$).

$\delta\varepsilon = Nk$ must be less than average distance $\Delta\varepsilon$ between them.

The other limit is to regard U as the perturbation, rather than k . In this case, the width of the one-particle crossing is k and is not affected by the many-body interaction, as long as the span $NU \ll k$. Using these criteria, we can define three different regimes (as can be seen in Fig. 5.3)

$$\begin{array}{ll}
 u \ll 1 & \text{mega crossing regime} \\
 1 < u < N^2 & \text{gradual crossing regime} \\
 u \gg N^2 & \text{sequential crossing regime}
 \end{array} \tag{5.13}$$

In the mega crossing regime (Fig. 5.3a), all of the particles move like one huge ball from one trap to the other. On the other extreme, in the sequential regime (Fig. 5.3c) the bosons move one at a time from one well to the other. The transition between these two regimes is dubbed the gradual crossing regime, as shown in Fig. 5.3b. The dynamics in the sequential and mega crossing regimes is fairly well understood. Therefore, we focused our studies on the intermediate regime, which combines attributes of both the mega and sequential regimes.

5.4.2 Rate-dependent Regimes

In addition to the u -dependent regimes, the rate of change of the bias defines three dynamical scenarios: adiabatic, diabatic, and sudden.

If we are changing our bias very slowly, we are in the adiabatic regime. In this case, we follow the uppermost energy level throughout our evolution, as shown in Fig. 5.4a. Thus we begin, as always, with all of our bosons in the left well $|N, 0\rangle$ and end with all of our bosons in the right well $|0, N\rangle$. The probability to stay adiabatic is determined by the Landau-Zener transition probability discussed in Chapter 4, i.e. the probability to remain in the highest energy level is $P_{ad} = 1 - P_{LZ}$.

On the other hand, we can drive our system very rapidly, causing it to tunnel from the highest energy level at the beginning of our evolution, to the lowest at the end (see Fig. 5.4c). We define this scenario as the sudden regime. In this case, rather than tunneling from one site to the other, as in the adiabatic scenario, the bosons stay put; therefore our final state is $|N, 0\rangle$.

Finally, we can drive the system at some intermediate rate, which lands us in what we designate as the diabatic scenario, as in Fig. 5.4b. Instead of ending with all bosons on one or the other site, in the diabatic regime the final state is more generic $|n, N - n\rangle$. The dynamics in this regime is, as in the adiabatic case, governed by Landau-Zener transitions. As can be seen in the energy level diagram for the gradual crossing regime (Fig. 5.3b), the gap between the energy levels changes as we move through the avoided crossings towards the lowest energy levels (the sea). Since these changing gaps determine P_{LZ} , the dynamics in diabatic scenario is not as simple to calculate as in the adiabatic scenario.

5.5 Results

In this section we will present the outcomes of our recent investigation into the occupation statistics of a BEC loaded in a driven double well potential. Our presentation

5 Dynamics of the Driven Dimer

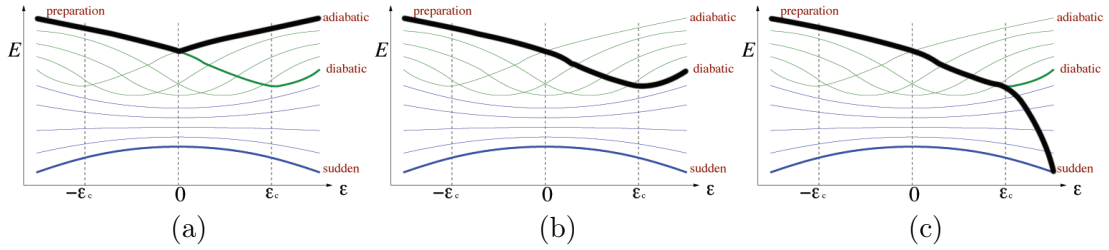


Figure 5.4: Energy level schematic in the gradual crossing regime. (a), (b), and (c) show the evolution of the system through the energy levels for the adiabatic, diabatic, and sudden scenarios, respectively.

follows that of our recent paper, Ref. [47], very closely.

5.5.1 Numerical Results

Our simulations are based on the numerical integration of the time-dependent Schrödinger equation

$$i\dot{\psi}_n = [-\varepsilon n + U(n^2 - Nn)]\psi_n - \frac{k}{2} \left[\sqrt{n(n_2+1)}\psi_{n+1} + \sqrt{n_2(n+1)}\psi_{n-1} \right] \quad (5.14)$$

where $n_2 = N - n$ and $\psi_n(t) = \langle n | \psi(t) \rangle$. We assume that initially all the atoms are on the left site, i.e. $|\psi(t=0)\rangle = |N, 0\rangle$. For the numerical integration, we used a fourth order Runge-Kutte scheme, choosing our time steps such to ensure that our norm $\sum_n |\psi_n(t)|^2$ is conserved to within 10^{-6} .

As stated earlier, the focus of our studies rests on the gradual crossing regime. In Fig. 5.5 we present a three-dimensional overview of the evolving $P_n(t)$ for 30 bosons with $u = 4.05$ and a rate $\dot{\varepsilon} = 10$. Fig. 5.6a (red) shows the mean occupation probability defined as: $\langle n \rangle = \sum_n |\psi_n(t)|^2 n$. While this is a global measure of the evolving occupation statistics, the variance $Var(n) = \langle n^2 \rangle - \langle n \rangle^2$ provides more refined information on $P_n(t)$. For an intermediate rate, placing us in the diabatic scenario, the $\langle n \rangle$ and the $Var(n)$ jump suddenly at a time which corresponds to $\varepsilon = 0$ (see Fig. 5.6a). This first jump occurs when the state comes across the first avoided crossing in our energy level spectrum. The subsequent changes in $\langle n \rangle$ and $Var(n)$ correspond to the other avoided

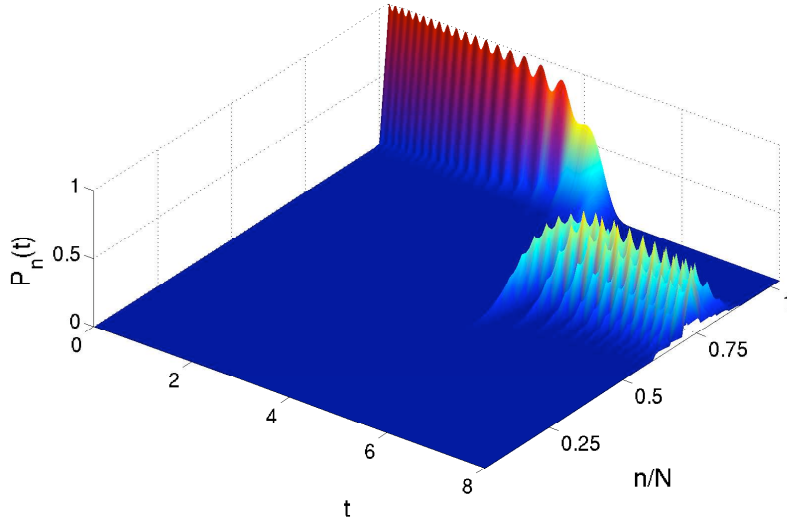


Figure 5.5: The evolution of the occupation statistics $P_n(t)$ for $u = 4.05$ and $\dot{\epsilon} = 10$.

crossings. The variance is shown in Fig. 5.6a (red). The semiclassical results for the $\langle n \rangle$ and $Var(n)$ are shown in black in Fig. 5.6a. We can clearly see that there is good agreement between the semiclassical and quantum calculations, which further cements our trust in the semiclassical approach.

However, as in the wavepacket dynamics case, our goal is to understand the full occupation statistics. Therefore, we would like to see how well the semiclassical theory matches the quantum for $P_n(t)$ in the driven system. In Fig. 5.6b, we show the semiclassical and quantum results for $P_n(t)$ for three distinct times - right before the jump in $\langle n \rangle$ (corresponding, in this case, to $t = 2$), during the jump (corresponding to $t = 2.08$), and well after the jump (corresponding to $t = 4$). Note that, for example, the asymmetry of $P_n(t = 2.08)$ cannot be captured by the binomial distribution, thus reconfirming that the mean-field approach will not be able to model the dynamics of the driven system. As the binomial distribution can be characterized by its spreading, we can designate deviations from it by comparing the probability spreadings: if the spreading of $P_n(t)$ is smaller/larger than that of the mean-field, we refer to it as sub-/super-binomial. We also note that any deviations from the binomial distribution are induced by the interatomic

5 Dynamics of the Driven Dimer

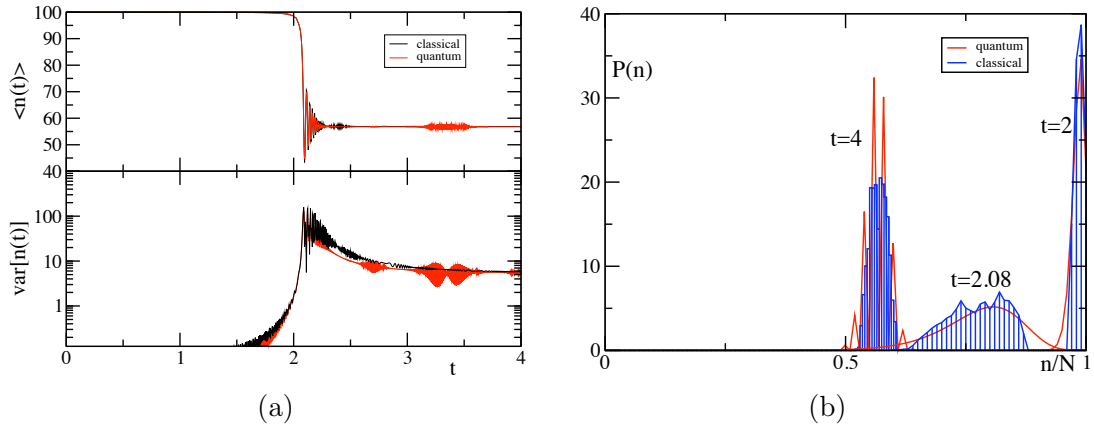


Figure 5.6: (a) Asymptotic evolution of $\langle n \rangle$ and $Var(n)$ for the semiclassical and quantum methods. (b) Occupation statistics (semiclassical and quantum) for just before the drop in $\langle n \rangle$ ($t = 2$), during the drop ($t = 2.08$), and long after the drop ($t = 4$).

interactions in our system.

Next, we address the effect of separatrix motion on $P_n(t)$ in the bias-sweep scenario. As we vary ε , the separatrix changes. Note that this separatrix motion cannot be avoided: For $\varepsilon < -\varepsilon_c$ the wavepacket is localized in the upper level. When $\varepsilon = -\varepsilon_c$, the separatrix emerges. As long as $-\varepsilon_c < \varepsilon < 0$ the wavepacket remains trapped on top of the big island, which gradually shrinks. When ε becomes larger than zero, the wavepacket can partially tunnel out from the shrinking island to the levels of the expanding island. When $\varepsilon = \varepsilon_c$, the shrinking island disappears and the remaining part of the wavepacket is squeezed out along the $n = n_c$ contour. We observe that the stretching along the separatrix during the nonlinear LZ transition is accompanied by narrowing in the transverse direction. This leads to a sub-binomial distribution $P_n(t)$ at the end of the sweep.

A summary of our numerical results for the asymptotic mean occupation $\langle n \rangle$ and variance $Var(n)$ are shown in Fig. 5.7. We also plot the participation number PN , which is another measure of the spreading of $P_n(t)$. The participation number is defined

5 Dynamics of the Driven Dimer

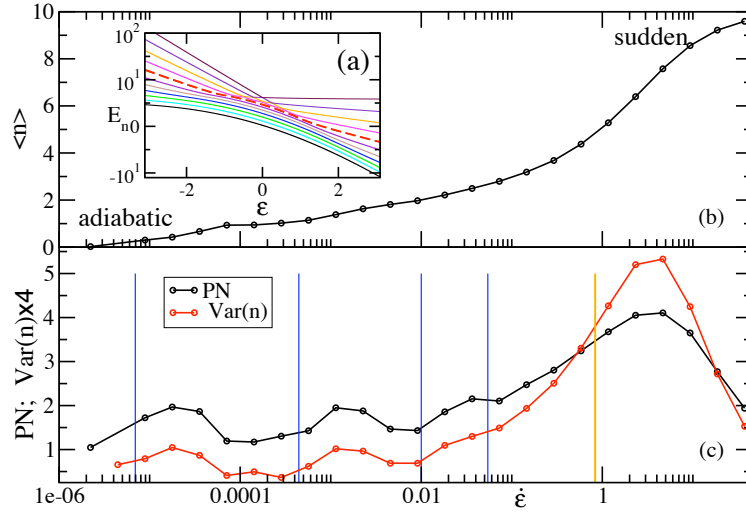


Figure 5.7: (a) Parametric evolution of the adiabatic energy levels versus the changing bias for $N = 10$ particles and $u = 2.5$. We have chosen units of time such that $k = 1$. The dashed line corresponds to the level $n_c = 4$. (b) Average occupation $\langle n \rangle$ versus the sweep rate $\dot{\epsilon}$. (c) Participation number (PN) and $Var(n)$ versus $\dot{\epsilon}$. The vertical lines indicate the various adiabatic (blue) and diabatic (orange) thresholds.

as:

$$PN \equiv \left(\sum_n P_n(t)^2 \right)^{-1} \quad (5.15)$$

Both the variance and the participation number provide significantly more information regarding the nature of the crossing process than the $\langle n \rangle$. As stated earlier, for very slow rates, the wavepacket follows a strict adiabatic process and ends at $n=0$, i.e. all particles have moved from site one to site two. For such slow rates, the system remains in the higher energy level throughout the driving process, thus leading one to expect that $P_n(t)$ will have a very narrow shape (and therefore a small $Var(n)$). For a moderate sweep rate the wavepacket ends in a superposition of $n=0$ and $n=1$ states, indicated by $PN = 2$. The widths of the avoided crossings of the energy levels get wider as we move to lower energy levels (see 5.5.2). At a very slow rate, the wavepacket will stay in the highest energy level (the adiabatic case). As we increase the rate, we will see a spreading in $P_n(t)$ due to a probability to be in the highest and in the second-highest

energy levels. If we step up the rate a bit more, we will be going too fast to stay in the highest energy level, but too slow to tunnel through the next, wider, avoided crossing. Thus, the wavepacket ends in the second-highest energy level and its profile is narrow. So, by looking at the oscillations in the variance and PN , we can resolve the possibility of ending in $n=1$, $n=2$, or $n=3$, as well as superpositions thereof. In the case shown in Fig. 5.7, the critical energy level is $n_c \approx 4$. For larger sweep rates, we observe a qualitatively different behavior that can be described as a crossover from an adiabatic/diabatic behavior to a sudden behavior at the peak value $PN = 4$. Therefore, we can use the variance to study all three regimes: adiabatic, diabatic, and sudden.

5.5.2 Theoretical Considerations

In Fig. 5.8 we summarize the borders of the three regimes (adiabatic/diabatic/sudden) in the two-dimensional parameter space $(u, \dot{\epsilon})$. The various borders follow from the breakdown of the adiabatic condition Eq. (4.12) that can be written as

$$\dot{\epsilon} \ll \omega_{osc}^2/\kappa \tag{5.16}$$

where ω_{osc} is a characteristic frequency of the unperturbed dynamics and κ is the coupling parameter that determines the rate of the driven transitions.

In the strict quantum adiabatic framework, ω_{osc} is simply the level spacing and κ is determined by the slopes of the intersecting levels. In order to determine the adiabatic thresholds in Fig. 5.7 we observe that for the intersection of the 0th level with the $(N - n)$ level the difference in slope is $\kappa = (N - n)$, because asymptotically (as can be seen from Eq. (3.17))

$$d(E_n - E_m)/d\mathcal{E} \sim (n - m). \tag{5.17}$$

In the absence of interaction ($u \ll 1$), the level spacing is $\omega_{osc} = k$ and only nearby levels are coupled, leading to the standard Landau-Zener adiabaticity condition $\dot{\epsilon} \ll k^2$. With strong interaction there is an N th order coupling between the $n = 0$ level and the

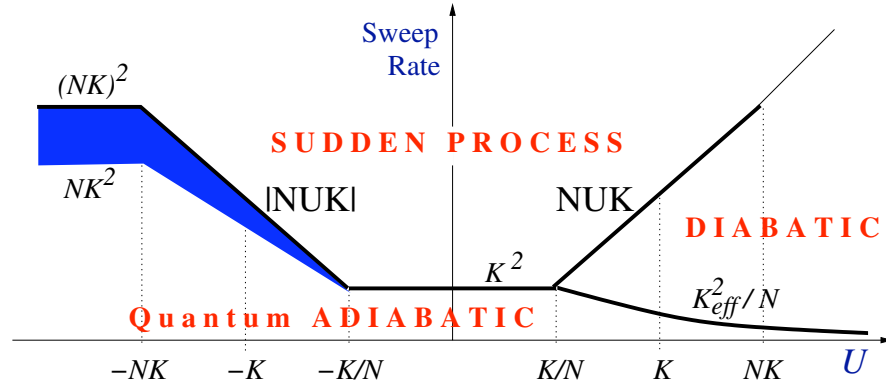


Figure 5.8: Diagram of the $(U, \dot{\epsilon})$ regimes. In the Rabi regime $|U| < k/N$, we have a crossover from adiabatic to sudden behavior. For $U < -k/N$, we have a broad crossover from adiabatic gradual (or sequential [24]) behavior to sudden behavior. For $U > k/N$, we have two crossovers: the first from the quantum adiabatic to the diabatic and a second from the diabatic to the sudden regime. For $U > Nk$, the distinction between the diabatic and the sudden regime is blurred because the final state is the same $(|N, 0\rangle)$.

$n = N$ level, which allows tunneling from the top of one island to the top of the other.

As discussed in §3.1 an estimate for this coupling is [27]

$$k_{eff} = \frac{NK}{[2^{N-1}(N-1)!]} \left(\frac{k}{U}\right)^{N-1}. \quad (5.18)$$

For a very small rate $\dot{\epsilon}$, i.e. in the adiabatic regime, the dynamics is determined by u and is described by the parametric evolution of the energy levels in mega, gradual, and sequential crossing regimes (see Ref. [24]).

For large N it may be impossible, in practice, to satisfy the strict adiabatic condition. In this case, the relevant mechanism for transition, i.e. the emission to the level n_c as described in the previous section, becomes semiclassical. In the limit $u \gg 1$, the emission to n_c is governed by the oscillation frequency $\omega_{osc} \sim \sqrt{|NUK|}$. This frequency determines the level spacing of the lower energy levels and also describes the level spacing in the vicinity of the separatrix, apart from some logarithmic corrections [7]. It follows that the diabatic-sudden crossover involves the threshold condition $\dot{\epsilon} \sim |NUK|$ as indicated in Fig. 5.8 and in Fig. 5.7 for the specific parameters of the simulations.

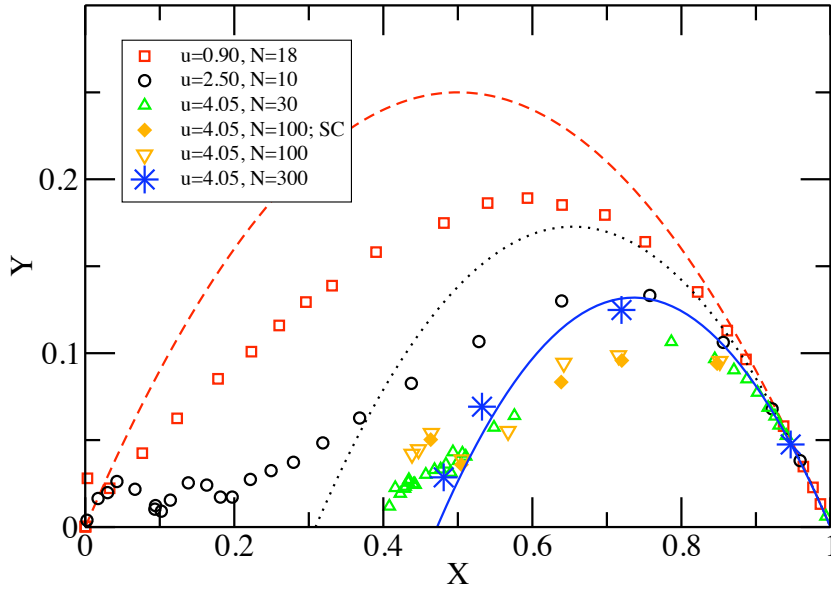


Figure 5.9: Sub-binomial scaling relation between $\langle n \rangle$ and $Var(n)$. The symbols correspond to numerical data plotted via the relations $Y = Var(n)/N$ and $X = \langle n \rangle / N$. The dashed, dotted, and solid lines indicate the standard binomial scaling ($u = 0$) and sub-binomial scaling [Eq. (5.20)] for $u = 2.5$ and $u = 4.05$, respectively. We also plot the results of semiclassical simulations (SC) for $N = 100$.

5.5.3 Scaling Relation between $\langle n \rangle$ and $Var(n)$

Due to the squeezing along the separatrix, the spreading of the wavepacket for an idealized diabatic process becomes negligible in the transverse direction. The diabatic-sudden crossover is related to the non-adiabatic transitions between the remaining $(N - n_c)$ sea levels, where nonlinear effects are negligible. It follows that the spreading can be approximately modeled by the toy Hamiltonian

$$H = B(t) \cdot J, \quad (5.19)$$

where J is a spin entity with $j_{eff} = (N - n_c)/2$, and $B(t)$ is a field with constant magnitude $|B(t)| = \Omega_0$ corresponding to the mean-level spacing. The sweep is like a rotation of $B(t)$ in the plane with some angular rate ω (see Appendix D). For such a (linear) model the mean-field approximation is exact and therefore we suggest (due to

5 Dynamics of the Driven Dimer

the truncation of Hilbert space) a sub-binomial rather than binomial scaling relation between the mean and the variance of the occupation statistics:

$$Y = (1 - X) \frac{X - c}{1 - c} \quad (5.20)$$

where $c = n_c/N$ and $n_c \approx (1 - u^{-2/3})^{3/2} N$. Our numerical data is reported in Fig. 5.9 via the relations $X = \langle n \rangle / N$ and $Y = \text{Var}(N) / N$ together with the binomial (zero interaction case) and sub-binomial scaling relation Eq. (5.20). We also plot the results of semiclassical simulations to further demonstrate the accuracy of the semiclassical method. The numerics confirm the expected u -dependent crossover from binomial to sub-binomial statistics, where the latter, with no fitting parameters, sets a lower bound for the variance. In addition, we can see that the agreement between the scaling and the numerics becomes better as the number of bosons in the system is increased.

The sub-binomial scaling relation between the $\langle n \rangle$ and $\text{Var}(n)$ will be especially useful to experimentalists. If an experimentalist measures the average atomic population and its variance, the scaling relation will allow her to determine the critical energy level and thus the interatomic interaction strength. Knowledge of the former could also be used to further explore controlling the flow of atoms from one well to another

6 Conclusions

We have investigated the effects of interatomic interactions on the full occupation statistics of a Bose-Einstein condensate of ultra-cold atoms loaded in a driven double well potential. Such a study provides information on fundamental questions like the applicability of semiclassical analysis to describing full occupations statistics, while also giving us some insight into the fluctuations (noise) in mesoscopic transport of many-body systems with interacting particles.

After finding that the mean-field approach focused on by the literature was not a viable theory to describe quantum dynamics on long time scales, we explored a semiclassical method. By studying the wavepacket dynamics of the symmetric dimer as well as the dynamics of the driven dimer, we were able to confirm that semiclassical methods are capable of modeling the full occupation statistics in both cases. Our approach can easily be generalized to more demanding set-ups, such as a BEC in longer optical lattices, where classically chaotic dynamics can be present.

Using a combination of classical, semiclassical, and quantum calculations, we were able to create a regime diagram identifying various $(U, \dot{\epsilon})$ dynamical regimes. These different dynamical behaviors are reflected in the structure of the asymptotic occupation distribution $P_n(t \rightarrow \infty)$. Specifically, if $|\psi\rangle = |0\rangle$, we are in the adiabatic regime; if $|\psi\rangle = |N\rangle$, we are in the sudden regime; and if $|\psi\rangle = |n\rangle$, we are in the diabatic regime.

Finally, we found a sub-binomial scaling relation between the average population and its variance. The resulting scaling depends only on $u = UN/k$, thus highlighting the importance of interatomic interactions in studying noise. The scaling relation became

6 Conclusions

more accurate in the semiclassical limit (where most current experiments operate), making it a potentially useful tool to experimentalists. If, for example, an experimentalist measures the $\langle n \rangle$ and $Var(n)$ of their system, our relation can be used to determine the interatomic interaction. Also, if the experimentalist knows the interatomic interaction U , then the relation can be used to estimate the level of noise (i.e. variance) present in the transport process.

The analysis of occupation statistics is very closely related to the problem of counting statistics in mesoscopic physics. Our results are one of the very few concrete examples where the whole occupation statistics were analyzed as well as the effects of many-body interactions on noise. Such a study will shed new light on the ongoing investigations of shot noise in the frame of electronic mesoscopic systems.

A Critical Bias

We calculate the critical bias discussed in §3.3 as follows. To remind, the energy of the system along $\varphi = 0$ is

$$E(\theta) \propto \frac{1}{2}u \cos^2 \theta - \frac{\varepsilon}{k} \cos \theta - \sin \theta. \quad (\text{A.1})$$

Its first and second derivatives are

$$E'(\theta) = \frac{1}{2}u \sin(2\theta) + \varepsilon/k \sin \theta - \cos \theta \quad (\text{A.2a})$$

$$E''(\theta) = -u \cos(2\theta) + \varepsilon/k \cos \theta + \sin \theta \quad (\text{A.2b})$$

To solve for the critical bias, we need solve $E'(\theta) = E''(\theta) = 0$. This equivalence leads to a set of equations

$$\sin(\theta)E''(\theta) - \cos(\theta)E'(\theta) = 1 + u \sin^3 \theta = 0 \quad (\text{A.3a})$$

$$\cos(\theta)E''(\theta) - \sin(\theta)E'(\theta) = \varepsilon/k - u \cos^3 \theta = 0 \quad (\text{A.3b})$$

which lead to the solutions

$$\theta_X = -\arcsin \left[\left(\frac{1}{u} \right)^{1/3} \right]; \quad \varepsilon_c = k \left(u^{2/3} - 1 \right)^{3/2} \quad (\text{A.4})$$

giving us the critical bias and the location of the WEST side saddle.

B Classical Analysis of Wavepacket Dynamics

In this appendix we aim to derive the frequency ω_{osc} describing the oscillations in population imbalance in the self-trapping regime. We start our analysis by defining the density matrix: $\rho_{lk} = A_l A_k^*$. Note that $\rho_{ll} = A_l A_l^*$ is the normalized number of particles at site l ; with the normalization defined such that: $\rho_{11} + \rho_{22} = 1$. The population imbalance is then written as $\rho = \rho_{11} - \rho_{22} = (n_1 - n_2)/N$, where n_1 and n_2 are the number of particles at sites 1 and 2, respectively, and N is the total number of atoms. In the calculations below we assume, without loss of generality, that $\varepsilon_i = 0$.

Subtracting Eq. (2.20) times A_j^* from its complex conjugate times A_l , we find that

$$i\dot{\rho}_{lj} = \tilde{U}\rho_{lj}(\rho_{ll} - \rho_{jj}) - \frac{k}{2}(\rho_{l+1,j} - \rho_{l,j+1} + \rho_{l-1,j} - \rho_{l,j-1}). \quad (\text{B.1})$$

Four different possible expressions can be derived from Eq. (B.1) from the cases: (a) $l = 1, j = 2$, (b) $l = 2, j = 1$, (c) $l = 1, j = 1$, and (d) $l = 2, j = 2$:

$$\begin{aligned} \dot{\rho}_{12} &= -i\tilde{U}\rho\rho_{12} - i\frac{k}{2}\rho, & \text{for } l = 1, j = 2 & \quad (a) \\ \dot{\rho}_{21} &= i\tilde{U}\rho\rho_{21} + i\frac{k}{2}\rho, & \text{for } l = 2, j = 1 & \quad (b) \\ \dot{\rho}_{11} &= -i\frac{k}{2}(\rho_{12} - \rho_{21}), & \text{for } l = 1, j = 1 & \quad (c) \\ \dot{\rho}_{22} &= i\frac{k}{2}(\rho_{12} - \rho_{21}), & \text{for } l = 2, j = 2. & \quad (d) \end{aligned} \quad (\text{B.2})$$

Adding Eqs. (B.2c) and (B.2d) we find that

$$\dot{\rho}_{11} + \dot{\rho}_{22} = 0 \quad (\text{B.3})$$

indicating that $\rho_{11} + \rho_{22}$ is a constant of motion. Therefore, since at $t = 0$, we know that $\rho_{11} + \rho_{22} = 1$, we are able to conclude that the total number of particles is conserved throughout the time evolution. The time derivative of the population imbalance is derived by taking the difference between Eq. (B.2c) and Eq. (B.2d),

$$\dot{\rho} = \dot{\rho}_{11} - \dot{\rho}_{22} = -ik(\rho_{12} - \rho_{21}). \quad (\text{B.4})$$

By adding Eq. (B.2a) and (B.2b) and substituting in for $\dot{\rho}$, we find

$$\dot{\rho}_{12} + \dot{\rho}_{21} = \frac{\tilde{U}}{2k}\rho\dot{\rho}, \quad (\text{B.5})$$

which simplifies to

$$\dot{\rho}_{12} + \dot{\rho}_{21} = \frac{\tilde{U}}{2k} \frac{d\rho^2}{dt}. \quad (\text{B.6})$$

B Classical Analysis of Wavepacket Dynamics

When we integrate both sides of this equation over time, we find

$$\rho_{12}(t) + \rho_{21}(t) = \frac{\tilde{U}}{2k}[\rho^2(t) - \rho^2(0)] + [\rho_{12}(0) + \rho_{21}(0)]. \quad (\text{B.7})$$

Then we add Eq. (B.2a) and (B.2b) and again substitute in for $\dot{\rho}$:

$$\ddot{\rho} = -\tilde{U}k\rho(\rho_{12} + \rho_{21}) + (ik)^2\rho. \quad (\text{B.8})$$

Keeping in mind that ρ is dependent on t , via Eq. (B.7) this becomes

$$\ddot{\rho}(t) = -\frac{\tilde{U}^2}{2}\rho^3(t) + \left(\frac{\tilde{U}^2}{2}\rho^2(0) - \tilde{U}k(\rho_{12}(0) + \rho_{21}(0)) + (ik)^2 \right) \rho(t), \quad (\text{B.9})$$

which is simply a differential equation,

$$\ddot{\rho}(t) = -A\rho^3(t) + B\rho(t), \quad (\text{B.10})$$

with constants $A = \tilde{U}^2/2$ and $B = \frac{\tilde{U}^2}{2}\rho^2(0) - \tilde{U}k(\rho_{12}(0) + \rho_{21}(0)) - k^2$. When we start with all bosons in the left well, $B = \tilde{U}^2/2 - k^2$.

By assigning the population imbalance a meaning analogous to the position of a particle of mass $m = 1$, we can interpret the right-hand side of Eq. (B.10) as a nonlinear force F responsible for the motion of the particle. Therefore, the underlying potential is $\mathcal{U}(\rho) = -\int F d\rho$. Integrating over ρ , this becomes

$$\mathcal{U}(\rho) = \frac{A}{4}\rho^4(t) - \frac{B}{2}\rho^2(t). \quad (\text{B.11})$$

We determine the zeroes of $\frac{\partial\mathcal{U}(\rho)}{\partial\rho}$ to find the maxima and minima of $\mathcal{U}(\rho)$:

$$\rho = \begin{cases} 0 \\ \pm\sqrt{\frac{B}{A}} \end{cases} \quad \text{only if } B > 0. \quad (\text{B.12})$$

At the minima, the double derivative $\frac{\partial^2\mathcal{U}(\rho)}{\partial\rho^2}$ takes on the values $\mathcal{U}''(\pm\sqrt{B/A}) = 2B$.

In order to capture ω_{osc} on the north pole when $u \gg 1$ (see §3.3), we take the limit $k \ll UN$, thus $B \approx \tilde{U}^2/2$. Therefore, $\mathcal{U}''(\pm\sqrt{B/A}) = \tilde{U}^2$.

Integrating Eq. (B.10) over ρ , we find

$$\frac{1}{2}\frac{\partial}{\partial\rho}\dot{\rho}^2 + \mathcal{U} = c_1 \quad (\text{B.13})$$

where c_1 is a constant of integration. We can expand $\mathcal{U}(\rho)$ about $\rho_0 = \pm\sqrt{B/A}$:

$$\frac{1}{2}\dot{\rho}^2 + \frac{1}{2}(\rho - \rho_0)^2\mathcal{U}''(\rho_0) = c_1 - \mathcal{U}(\rho_0) \quad (\text{B.14})$$

This is the equation for the harmonic oscillator with frequency $\omega_{osc} = NU$, which governs the small oscillations of the population imbalance in the self-trapping regime.

C The Equivalence of Counting and Occupation Statistics in the Dimer

In many site systems, counting statistics and occupation statistics are not necessarily equivalent. As the names themselves imply, occupation statistics are related to how many bosons are on each lattice site, while counting statistics correspond to the number of bosons which tunnel through a specific path from one site to another. Intuitively, these quantities are analogous to one another in the two site system. In this appendix, we will show, via the simplest model of a single particle in a double well potential, that this is, in fact, true [10]. The single particle system has no interatomic interactions, thus the Hamiltonian is

$$H = \begin{bmatrix} \dot{\epsilon}t/2 & k/2 \\ k/2 & -\dot{\epsilon}t/2 \end{bmatrix}. \quad (\text{C.1})$$

We can define two operators which will allow us to define occupation versus counting statistics. The first is the occupation operator \hat{N} , which counts all of the bosons in the left well, and the second is the current operator \hat{I}

$$\hat{N} = \begin{bmatrix} 0 & 0 \\ 0 & 1 \end{bmatrix}; \quad \hat{I} = \begin{bmatrix} 0 & i\frac{k}{2} \\ -i\frac{k}{2} & 0 \end{bmatrix} \quad (\text{C.2})$$

The current operator can be used to define a counting operator \hat{Q}

$$\hat{Q} = \int_0^t \hat{I}(t') dt'. \quad (\text{C.3})$$

Since we are working with a dimer, the change in the number of particles on the first site must be equal to the flow of particles between the two sites, thus using the Heisenberg picture, we can state

$$\frac{d}{dt} \hat{N}(t) = \hat{I}(t). \quad (\text{C.4})$$

Utilizing this relation while integrating Eq. (C.3), we find that

$$\hat{Q} = \hat{N}(t) - \hat{N}(0). \quad (\text{C.5})$$

If we assume, as we do in our studies, that all of the particles begin on the left site, then we can conclude that

$$\langle \hat{Q}^m \rangle = \langle \hat{N}^m \rangle; \quad \text{where } m=1,2. \quad (\text{C.6})$$

In other words, the first and second moments of the occupation and counting statistics are equivalent.

D The Diabatic-Sudden Crossover

To gain a better understanding of the diabatic-sudden crossover in an N level system, we employ a toy Hamiltonian $H = B(t) \cdot J$, where J is a spin $j = N/2$ entity and $B(t)$ is a field with constant magnitude $B(t) = \Omega_0$, corresponding to the mean level spacing.

The spin is initially prepared in the $\theta = 0$ direction, where θ is the polar angle of the Bloch sphere. We initiate the dynamics by making a $\phi = \pi$ rotation of $B(t)$ at an angular rate ω in the $x-y$ plane. As a result, the spin rotates some angle Φ . In the case that ω is very small and we are in the adiabatic limit, $\Phi = \pi$. If, on the other hand, we are in the sudden limit (ω very large), $\Phi = 0$. For intermediate rates, we would like to find the phase lag $\Theta = \pi - \Phi$, in addition to Φ itself.

Without loss of generality, we can use the spin 1/2 equations in order to find the time-dependent orientation of the spin. The orientation is thus represented by

$$\psi^{(1)} = e^{-i\omega t/2} \left(c_1 e^{i\Omega t/2} + c_2 e^{-i\Omega t/2} \right) \quad (\text{D.1a})$$

$$\psi^{(2)} = \Omega_0 e^{i\omega t/2} \left(\frac{c_1}{\Omega + \omega} e^{i\Omega t/2} - \frac{c_2}{\Omega - \omega} e^{-i\Omega t/2} \right) \quad (\text{D.1b})$$

where ψ^n are spinors and $\Omega = \sqrt{\omega^2 + \Omega_0^2}$. For a steady state solution with $c_1 = 1$ and $c_2 = 0$, the orientation of the spin can be written as

$$|\psi(t)\rangle = \begin{bmatrix} \psi^{(1)} \\ \psi^{(2)} \end{bmatrix} = e^{i\Omega t} \left[e^{-i\omega t/2} \cos\left(\frac{\theta}{2}\right) |\uparrow\rangle + e^{i\omega t/2} \sin\left(\frac{\theta}{2}\right) |\downarrow\rangle \right] \quad (\text{D.2})$$

where $\theta = 2 \arctan [\Omega_0/(\Omega + \omega)]$. In the adiabatic limit, where $\omega \rightarrow 0$, the angle $\theta = \pi/2$. In the sudden limit, $\theta = 0$. At the end of the sweep of $B(t)$, $\Phi = 2\theta$. Defining $\alpha = \omega/\Omega_0$, we can write the phase lag as

$$\Theta(\alpha) = \pi - 4 \arctan \left(\frac{1}{\sqrt{1 + \alpha^2} + \alpha} \right). \quad (\text{D.3})$$

We can use the phase lag to help determine the various moments of the occupation (or spin direction) with

$$\langle \Theta | J_z^k | \Theta \rangle = \langle \uparrow | [\cos(\Theta) J_z + \sin(\Theta) J_x]^k | \uparrow \rangle \quad (\text{D.4})$$

D The Diabatic-Sudden Crossover

Moving back to the spin $N/2$ case, we find

$$\langle J_z \rangle = \frac{N}{2} \cos(\Theta) \quad (\text{D.5a})$$

$$\langle J_z^2 \rangle = \left(\frac{N}{2}\right)^2 \cos^2(\Theta) + \frac{N}{4} \sin^2(\Theta). \quad (\text{D.5b})$$

Therefore the variance is

$$\langle J_z^2 \rangle - \langle J_z \rangle^2 = \frac{N}{4} \sin^2(\Theta). \quad (\text{D.6})$$

Plugging the expression for Θ back in, we find that the expectation value and variance are

$$\langle n \rangle = N \frac{\alpha^2}{1 + \alpha^2} \quad (\text{D.7a})$$

$$\text{Var}(n) = N \frac{\alpha^2}{(1 + \alpha^2)^2}. \quad (\text{D.7b})$$

From these equations, we are able to see that there is a binomial relation between the variance and the expectation value. Defining $X = \langle n \rangle / N$ and $Y = \text{Var}(n) / N$, we can find that $Y = (1 - X)X$. This is the same scaling relation we would find for a BEC with no interatomic interactions in a driven double well potential.

Bibliography

- [1] Albiez, M., Gati, R., Folling, J., Hunsmann, S., Cristiani, M., and Oberthaler, M. K. Direct Observation of Tunneling and Nonlinear Self-Trapping in a Single Bosonic Josephson Junction. *Physical Review Letters* **95**, 010402 (2005).
- [2] Anderson, B. P. and Kasevich, M. A. Macroscopic Quantum Interference from Atomic Tunnel Arrays. *Science* **282**, 1686 (1998).
- [3] Anderson, M. H., Ensher, J. R., Matthews, M. R., Wieman, C. E., and Cornell, E. A. Observation of Bose-Einstein Condensation in a Dilute Atomic Vapor. *Science* **269**, 198 (1995).
- [4] Bernstein, L., Eilbeck, J. C., and Scott, A. C. The quantum theory of local modes in a coupled system of nonlinear oscillators. *Nonlinearity* **3**, 293 (1990).
- [5] Berry, M. V. The adiabatic limit and the semiclassical limit. *Journal of Physics A* **17** (1984).
- [6] Blanter, Y. M. and Büttiker, M. Shot noise in mesoscopic conductors. *Physics Reports* **336** (2000).
- [7] Boukobza, E., Chuchem, M., Cohen, D., and Vardi, A. Phase-diffusion dynamics in weakly coupled Bose-Einstein condensates. *arXiv:0812.1204* .
- [8] Budoyo, R. P. Conductance of Mesoscopic Rings (2008).
- [9] Cataliotti, F. S., Burger, S., Fort, C., Maddaloni, P., Minardi, F., Trombettoni, A., Smerzi, A., and Inguscio, M. Josephson Junction Arrays with Bose-Einstein Condensates. *Science* **293**, 843 (2001).
- [10] Chuchem, M. and Cohen, D. Restricted quantum-classical correspondence and counting statistics of a coherent transition. *Physical Review A* **77** (2008).
- [11] Chuchem, M., Smith-Mannschott, K., Cohen, D., and Kottos, T. (in preparation) (2009).
- [12] Cohen, D. and Kottos, T. Non-perturbative response: chaos versus disorder. *Journal of Physics A* **36** (2003).
- [13] Cohen-Tannoudji, C. N. Nobel lecture: Manipulating atoms with photons. *Rev. Mod. Phys.* **70**, 707 (1998).
- [14] Cohen-Tannoudji, C. N. and Phillips, W. D. New mechanisms for laser cooling. *Physics Today* **43**, p33 (1990).

Bibliography

- [15] Dalfovo, F., Giorgini, S., Pitaevskii, L. P., and Stringari, S. Theory of bose-einstein condensation in trapped gases. *Rev. Mod. Phys.* **71**, 463 (1999).
- [16] Davidson, N. Personal communication (2009).
- [17] Davis, K. B., Mewes, M. O., Andrews, M. R., van Druten, N. J., Durfee, D. S., Kurn, D. M., and Ketterle, W. Bose-Einstein Condensation in a Gas of Sodium Atoms. *Phys. Rev. Lett.* **75**, 3969 (1995).
- [18] Einstein, A. Quantentheorie des einatomigen idealen Gases. *Sitzungsberg. Preuss. Akad. Wiss., Phys. Math. K.* page 261 (1924).
- [19] Einstein, A. Quantentheorie des einatomigen idealen Gases - Zweite Ausgabe. *Sitzungsberg. Preuss. Akad. Wiss., Phys. Math. K.* page 3 (1925).
- [20] Estève, J., Gross, C., Weller, A., Giovanazzi, S., and K., O. M. Squeezing and entanglement in a bose-einstein condensate. *Nature* **445** (2008).
- [21] Hagley, E. W., Deng, L., Kozuma, M., Wen, J., Helmerston, K., Rolston, S. L., and Phillips, W. D. A Well-Collimated Quasi-Continuous Atom Laser. *Science* **283**, 1706 (1999).
- [22] Hansel, W., Hommelhoff, P., Hansch, T. W., and Reichel, J. Bose-einstein condensation on a microelectronic chip. *Nature* **413**, 498 (2001).
- [23] Hiller, M. Chaotic Quantum Dynamics, Irreversibility and the Applicability of Random Matrix Theory (2003).
- [24] Hiller, M., Kottos, T., and Cohen, D. Controlled quantum stirring of Bose-Einstein condensates. *Physical Review A* **78** (2008).
- [25] Hwang, J. and Pechukas, P. The adiabatic theorem in the complex plane and the semiclassical calculation of nonadiabatic transition amplitudes. *The Journal of Chemical Physics* **67** (1977).
- [26] Kalosakas, G. and Bishop, A. R. Small-tunneling-amplitude Boson-Hubbard dimer: Stationary states. *Phys. Rev. A* **65** (2002).
- [27] Kalosakas, G., Bishop, A. R., and Kenkre, V. M. Multiple-timescale quantum dynamics of many interacting bosons in a dimer. *J. Phys. B* **36**, 3233 (2003).
- [28] Kalosakas, G., Bishop, A. R., and Kenkre, V. M. Small-tunneling-amplitude boson-hubbard dimer. ii. dynamics. *Phys. Rev. A* **68**, 023602 (2003).
- [29] Ketterle, W. Nobel lecture: When atoms behave as waves: Bose-Einstein Condensation and the atom laser. *Rev. Mod. Phys.* **74**, 1131 (2002).
- [30] Kierig, E., Schnorrberger, U., Schietinger, A., Tomkovic, J., and Oberthaler, M. K. Single-Particle Tunneling in Strongly Driven Double-Well Potentials. *Physical Review Letters* **100** (2008).

Bibliography

- [31] Kumar, N. Bose-Einstein condensation: Where many become one and so there is plenty of room at the bottom. *Current Science* **89** (2005).
- [32] Leggett, A. J. Bose-Einstein Condensation in the Alkali Gases: Some fundamental concepts. *Rev. Mod. Phys.* **73**, 307 (2001).
- [33] Likharev, K. K. Superconducting weak links. *Rev. Mod. Phys.* **51**, 101 (1979).
- [34] Liu, J., Fu, L., Ou, B., Chen, S., Choi, D., Wu, B., and Niu, Q. Theory of nonlinear Landau-Zener tunneling. *Physical Review A* **66** (2002).
- [35] Longair, M. S. *Theoretical concepts in physics*. Cambridge University Press (1984).
- [36] Micheli, A., Daley, A. J., Jaksch, D., and Zoller, P. Single atom transistor in a 1d optical lattice. *Physical Review Letters* **93**, 140408 (2004).
- [37] Morsch, O. and Oberthaler, M. Dynamics of Bose-Einstein Condensates in Optical Lattices. *Rev. Mod. Phys.* **78**, 179 (pages 37) (2006).
- [38] Nordling, C. and Kastberg, A. The nobel prize in physics 1997.
- [39] Orzel, C., Tuchman, A. K., Fenselau, M. L., Yasuda, M., and Kasevich, M. A. Squeezed States in a Bose-Einstein Condensate. *Science* **291**, 010402 (2001).
- [40] Pereverzev, S. V., Loshak, A., Backhaus, S., Davis, J. C., and Packard, R. E. Quantum oscillations between two weakly coupled reservoirs of superfluid ^3He . *Nature* **388**, 449 (1997).
- [41] Sarpeshkar, R., Delbrück, T., and Mead, C. A. White Noise in MOS Transistors and Resistors. *IEEE Circuits and Devices Magazine* **9** (1993).
- [42] Schmiedmayer, J., Folman, R., and Calarco, T. Quantum information processing with neutral atoms on an atom chip. *Journal of Modern Optics* **49**, 1375 (2002).
- [43] Schumm, T., Hofferberth, S., Andersson, L. M., Wildermuth, S., Groth, S., Bar-Joseph, I., Schmiedmayer, J., and Kruger, P. Matter-wave interferometry in a double well on an atom chip. *Nat Phys* **1**, 57 (2005).
- [44] Shin, Y., Saba, M., Schirotzek, A., Pasquini, T. A., Leanhardt, A. E., Pritchard, D. E., and Ketterle, W. Distillation of Bose-Einstein Condensates in a Double-Well Potential. *Physical Review Letters* **92**, 150401 (2004).
- [45] Smerzi, A., Fantoni, S., Giovanazzi, S., and Shenoy, S. R. Quantum coherent atomic tunneling between two trapped bose-einstein condensates. *Phys. Rev. Lett.* **79**, 4950 (1997).
- [46] Smith-Mannschott, K. Counting Statistics of a Bose-Einstein Condensate in a Double-Well Potential (2008).
- [47] Smith-Mannschott, K., Chuchem, M., Hiller, M., Cohen, D., and Kottos, T. Occupation Statistics of a BEC for a Driven Landau-Zener Crossing. *under review by Physical Review Letters* (2009).

Bibliography

- [48] Stenger, J., Stamper-Kurn, D. M., Andrews, M. R., Chikkatur, A. P., Inouye, S., Miesner, H.-J., and Ketterle, W. Optically Confined Bose-Einstein Condensates. *J. Low Temp. Phys.* **113**, 167 (1998).
- [49] Stotland, A. and Cohen, D. Diffraction energy spreading and its semiclassical limit. *Journal of Physics A* **39** (2006).
- [50] Sukhatme, K., Mukharsky, Y., Chui, T., and Pearson, D. Observation of the ideal josephson effect in superfluid 4He. *Nature* **411**, 280 (2001).
- [51] Tiecke, T. G., Kemmann, M., Buggle, C., Shvarchuck, I., von Klitzing, W., and Walraven, J. T. M. Bose-Einstein condensation in a magnetic double-well potential. *Journal of Optics B: Quantum and Semiclassical Optics* **5**, S119 (2003).
- [52] Townsend, C., Ketterle, W., and Stringari, S. Bose-Einstein condensation. *Physics World* (1997).
- [53] Townsend, C., Ketterle, W., and Stringari, S. Bose-Einstein Condensation. *Physics World* (1997).
- [54] Weiss, U. *Quantum dissipative system*. World Scientific (2008).
- [55] Wilkinson, M. *Parametric random matrices: Static and dynamic applications*. Kluwer Academic/Plenum Publishers.
- [56] Witthaut, D., Graefe, E. M., and Korsch, H. J. Towards a generalized Landau-Zener formula for an interacting Bose-Einstein condensate in a two-level system. *Physical Review A* **73** (2006).
- [57] Wu, B. and Liu, J. Commutability between the Semiclassical and Adiabatic Limit. *Physical Review Letters* **96** (2006).
- [58] Wu, B. and Niu, Q. Nonlinear Landau-Zener tunneling. *Physical Review A* **61** (2000).
- [59] Zener, C. Non-Adiabatic Crossing of Energy Levels. *Proceedings of the Royal Society of London. Series A* **137**.